

STOCHASTIC GALERKIN METHOD FOR CLOUD SIMULATION

A. CHERTOCK, A. KURGANOV, M. LUKÁČOVÁ-MEDVIŠOVÁ, P. SPICHTINGER, AND B. WIEBE

ABSTRACT. We develop a stochastic Galerkin method for a coupled Navier-Stokes-cloud system that models dynamics of warm clouds. Our goal is to explicitly describe the evolution of uncertainties that arise due to unknown input data, such as model parameters and initial or boundary conditions. The developed stochastic Galerkin method combines the space-time approximation obtained by a suitable finite volume-finite method with a spectral-type approximation based on the generalized polynomial chaos expansion in the stochastic space. The resulting numerical scheme yields a second-order accurate approximation in both space and time and exponential convergence in the stochastic space. Our numerical results demonstrate the reliability and robustness of the stochastic Galerkin method for some typical atmospheric scenarios.

1. INTRODUCTION

Clouds constitute one of the most important component in the Earth-atmosphere system. They influence the hydrological cycle and by interacting with radiation they control the energy budget of the system. However, clouds are one of the most uncertain components, which, unlike the atmospheric flows, cannot be modeled using first principles of physics.

Clouds are composed by myriads of water particles in different phases (liquid and solid), and thus they need to be described by a large ensemble in a statistical sense. A common way of obtaining such an ensemble is by using a mass or size distribution, which would lead to a Boltzmann-type evolution equation. Although there are some approaches available in literature to formulate cloud models in such a way [4, 21, 22], a complete and consistent description is missing. Since measurements of size distributions of cloud particles are difficult, we are often restricted to averaged quantities such as, for example, mass of water per dry air (mass concentrations). Therefore, models are often formulated in terms of so-called bulk quantities, that is, mass and number concentrations of the respective water species. Many cloud processes are necessary to describe the time evolution of the cloud as a statistical ensemble, that is, particle formation or annihilation, growth/evaporation of particles, collision processes, and sedimentation due to gravity. For each of the processes, we have to formulate a representative mathematical term in the sense of a rate equation. Although for some processes the physical mechanisms are quite understood, the formulation of the process rates usually contain uncertain parameters, thus cloud models come with inherent uncertainty. On the other hand, the initial conditions for atmospheric flows and the embedded clouds are also not perfectly constrained, leading to uncertainties in the environmental conditions. It is well-known from former studies that uncertainties in cloud processes and in environmental conditions can lead to drastic changes in simulations, thus these uncertainties influence predictability of moist atmospheric flows, clouds and precipitation in a crucial way; for instance, the distribution of latent heat is changed, which in turn can influence frontogenesis [17] or convection [15, 29].

For investigations of the impact of these uncertain cloud model parameters as well as the impact of variations in environmental conditions on atmospheric flows, sensitivity studies are usually carried out. Since one or more parameters are (randomly) varied, the Monte Carlo approach can be used. This, however, requires a large ensemble of simulations to be conducted, which makes Monte Carlo methods computationally expensive and requires a very fine sampling of the parameter space and possible environmental conditions. We therefore choose a different way of representing random variations by using spectral expansions in the stochastic space. This approach enables us to investigate the impact of variations in cloud model parameters and initial conditions on the evolution of moist flows with embedded clouds.

We consider a mathematical model of cloud dynamics that consists of the Navier-Stokes equations coupled with the cloud evolution equations for the water vapor, cloud water and rain. In this model developed

in [27, 40] and presented in Section 2, the Navier-Stokes equations describe weakly compressible flows with viscous and heat conductivity effects, while microscale cloud physics is modeled by the system of advection-diffusion-reaction equations.

In this paper, we study a stochastic version of the coupled Navier-Stokes-cloud model in order to account for uncertainties in input quantities, such as model parameters, initial and boundary conditions, etc. Our main goal is to design an efficient numerical method for quantifying uncertainties in solutions of the studied system. In recent years, a wide variety of uncertainty quantification methods has been proposed and investigated in the context of physical and engineering applications. These methods include stochastic Galerkin methods based on generalized polynomial chaos (gPC) [9, 11, 14, 16, 18, 26, 39, 41, 45–48, 52], stochastic collocation methods [28, 44, 50, 51], and multilevel Monte Carlo methods [33–36, 43]. Each of these groups of methods has its own pros and cons. While results obtained by the Monte Carlo simulations are generally good, the approach is not very efficient due to a large number of realizations required. Stochastic collocation methods are typically more efficient than the Monte Carlo ones, since they only require solving the underlying deterministic system at the certain quadrature nodes in the stochastic space. These data are then used to reconstruct the gPC expansion using an appropriate set of orthogonal polynomials. Stochastic Galerkin methods offer an alternative approach for computing the gPC expansion. In general, they are more rigorous and efficient than the Monte Carlo and collocation ones; see, e.g., [12]. On the other hand, application of the stochastic Galerkin method requires changes in the underlying code, because in this approach one needs to solve a system of PDEs for the gPC expansion coefficients.

We develop a new stochastic Galerkin method for the coupled Navier-Stokes-cloud system. We restrict our consideration to the case in which the uncertainties are only in the cloud dynamics; extension to the full stochastic Navier-Stokes-cloud model is left to future studies. Thus, we need to solve the deterministic Navier-Stokes equations coupled with the PDE system for the gPC expansion coefficients for the cloud variables. Our numerical method is an extension of the approach proposed in [27] for the purely deterministic version of the coupled Navier-Stokes-cloud system. This method is based on the operator splitting approach, in which the system is split into the macroscopic Navier-Stokes equations and microscopic cloud model with random inputs. The Navier-Stokes equations are then solved by an implicit-explicit (IMEX) finite-volume method, while for the cloud equations we develop a stochastic Galerkin method based on the gPC. The resulting gPC coefficient system is numerically solved by a finite-volume method combined with an explicit Runge-Kutta method with an enlarged stability region [32].

The paper is organized as follows. We start in Section 2 with the description of the deterministic Navier-Stokes-cloud model. We then continue in Section 3 with the presentation of the stochastic model. Sections 4 and 5 are devoted to the numerical method for the deterministic and stochastic models, respectively. Finally, in Sections 6 and 7, we report on numerical experiments for well-known meteorological benchmarks—rising warm bubble and Rayleigh-Bénard convection—for the deterministic and stochastic models, respectively. Our numerical results clearly demonstrate that the proposed stochastic Galerkin method is capable of quantifying the uncertainties of complex atmospheric flows.

2. DETERMINISTIC MATHEMATICAL MODEL

We study a mathematical model of cloud dynamics, which is based on the compressible nonhydrostatic Navier-Stokes equations for moist atmosphere (that is, mixture of ideal gases dry air and water vapor),

$$\begin{aligned}
 \rho_t + \nabla \cdot (\rho \mathbf{u}) &= 0, \\
 (\rho \mathbf{u})_t + \nabla \cdot (\rho \mathbf{u} \otimes \mathbf{u} + p \text{Id} - \mu_m \rho (\nabla \mathbf{u} + (\nabla \mathbf{u})^\top)) &= -\rho g e_3, \\
 (\rho \theta)_t + \nabla \cdot (\rho \theta \mathbf{u} - \mu_h \rho \nabla \theta) &= S_\theta,
 \end{aligned} \tag{2.1}$$

and evolution equations for cloud variables,

$$\begin{aligned}(\rho q_v)_t + \nabla \cdot (\rho q_v \mathbf{u} - \mu_q \rho \nabla q_v) &= \rho(-C + E), \\(\rho q_c)_t + \nabla \cdot (\rho q_c \mathbf{u} - \mu_q \rho \nabla q_c) &= \rho(C - A_1 - A_2), \\(\rho q_r)_t + \nabla \cdot (-v_q \rho q_r \mathbf{e}_3 + \rho q_r \mathbf{u} - \mu_q \rho \nabla q_r) &= \rho(A_1 + A_2 - E).\end{aligned}\tag{2.2}$$

Here, ρ is the density, \mathbf{u} is the velocity vector, θ is the moist potential temperature, p is the pressure, g is the acceleration due to gravity, μ_m is the dynamic viscosity, μ_h the thermal conductivity, and μ_q the cloud diffusivity. We denote by t the time variable and by \mathbf{x} the space vector; $\mathbf{x} = (x_1, x_2, x_3)$ in the three-dimensional (3-D) and $\mathbf{x} = (x_1, x_3)$ in the two-dimensional (2-D) cases. Furthermore, $\mathbf{e}_3 = (0, 0, 1)^\top$ and $\mathbf{e}_3 = (0, 1)^\top$ in the 3-D and 2-D cases, respectively. We set $\mu_m = 10^{-3}$ and $\mu_h = 10^{-2} = \mu_q$. Note that the systems (2.1) and (2.2) are coupled through the source term S_θ , which represents the impact of phase changes and will be defined below, see (2.6). The temperature T can be obtained from the moist adiabatic ideal gas equation

$$T = \frac{R}{R_m} \theta \left(\frac{p}{p_0} \right)^{R_m/c_p},\tag{2.3}$$

where $p_0 = 10^5$ [Pa] is the reference pressure at sea level. In addition to the usual definition of a potential temperature, we use $R_m = (1 - q_v - q_c - q_r)R + q_v R_v$ with the ideal gas constant of dry air $R = 287.05$ [J/(kg·K)], the gas constant of water vapor $R_v = 461.51$ [J/(kg·K)] and the specific heat capacity of dry air for constant pressure $c_p = 1005$ [J/(kg·K)]. In order to close the system, we determine the pressure from the equation of state that includes moisture

$$p = p_0 \left(\frac{R \rho \theta}{p_0} \right)^{\gamma_m} \quad \text{with} \quad \gamma_m = \frac{c_p}{c_p - R_m}.\tag{2.4}$$

We note that in the dry case R_m reduces to R , $S_\theta = 0$ and the moist ideal gas equation as well as the moist equation of state become their dry analogon.

In this paper, we restrict our investigations to clouds in the lower part of the troposphere, that is, to clouds consisting of liquid droplets exclusively. All of the processes involving ice particles are left for future research. For the representation of liquid clouds in our model we use the so-called single moment scheme, that is, equations for the bulk quantities of mass concentrations of different water phases. For the representation of the relevant cloud processes we adapt a recently developed cloud model [40]. Note that for bulk models, the process rates cannot be derived completely from first principles. Consequently, some uncertain parameters show up naturally. This underlies the need of a rigorous sensitivity study which is the goal of the present paper.

Generally, we follow the standard approach in cloud physics modeling for separating hydrometeors of different sizes, as firstly introduced in [19]. This relies on the observations that small droplets have a negligible falling velocity. In addition, measurements indicate two different modes of droplets in the size distribution, which can be associated to small cloud droplets and large rain drops [49]. Thus, we use the cloud variables q_c and q_r indicating mass concentration of (spatially stationary) cloud droplets and (falling) rain drops, respectively, and the water vapor concentration q_v , that is,

$$q_\ell = \frac{\text{mass of dry air}}{\text{mass of the respective phase}} \quad \text{for} \quad \ell \in \{v, c, r\}.$$

The rest of this section is devoted to a description of the different terms on the right-hand side (RHS) of (2.2), which represents the following relevant cloud processes.

- *Condensation/evaporation of cloud droplets*

Cloud droplets can be formed by the activation of so-called cloud condensation nuclei. Liquid aerosol particles can grow by water vapor uptake to larger sizes; this effect can be described by the Köhler theory; see, e.g., [23, 38]. As described in detail in [40], we represent the cloud droplet number concentration n_c by a nonlinear relationship

$$n_c = \frac{8 \cdot 10^8 q_c}{q_c + 1.68 \cdot 10^6} \coth \left(\frac{q_c}{2.1} \right).$$

Growth and evaporation of small cloud particles are dominated by diffusion processes. If the water vapor concentration q_v is larger than the equilibrium water vapor concentration $q_* = q_*(p, T)$, water molecules diffuse to the water droplet and thus the cloud particle is growing. For $q_v < q_*$, the water droplet is evaporating. These effects are represented in the terms C and E . In particular,

$$C = C_1 + C_{\text{act}} \quad \text{with} \quad C_1 = 0.7796DG(q_v - q_*) \left(\frac{8 \cdot 10^8}{q_c + 1.68 \cdot 10^6} \coth\left(\frac{q_c}{2.1}\right) \right)^{2/3} \rho q_c \quad (2.5)$$

$$\text{and} \quad C_{\text{act}} = 1.2566 \cdot 10^{-3} DG \rho (q_v - q_*)_+,$$

where

$$D = D(p, T) = 2.11 \cdot 10^{-5} (T/273.15)^{1.94} (101325/p),$$

$$G = G(p, T) = \left[(2.53 \cdot 10^6 / 461.52T - 1) 2.53 \cdot 10^8 p_s D / 461.52KT^2 + 1 \right]^{-1},$$

$$p_s = p_s(T) = \exp \left\{ 54.842763 - 6763.22/T - 4.21 \ln T + 0.000367T + \tanh(0.0415(T - 218.8)) \right. \\ \left. \cdot (53.878 - 1331.22/T - 9.44523 \ln T + 0.014025T) \right\},$$

$$K = K(T) = \frac{0.02646T^{3/2}}{T + 245.4 \cdot 10^{-12/T}}, \quad q_* = q_*(p, T) = \frac{0.622p_s}{p}.$$

Note that since cloud droplets are activated for water vapor concentrations larger than the thermodynamic equilibrium ($q_v > q_*$) the term C_{act} is added as a source of liquid water in (2.5).

We introduce an additional closure for the number concentration of rain drops $n_r = c_r q_r^{\alpha_r}$, which is explicitly used in [40]. Under the assumption that the size of rain drops is distributed to an exponential law; see, e.g., [30], we obtain the exponent $\alpha_r = 1/4$. Note that this relation will be inserted in any formulation of cloud process rates, involving n_r . Finally, the evaporation of rain drops is changed by hydrodynamic effects of air motions around the drops. This is corrected by an additional empirical relationship. The final formulation of the evaporation rate E is given by

$$E = -0.7796DG(q_* - q_v)_+ \left(644.5198\sqrt{\rho q_r} + 17.5904D^{-1/3}\sqrt{\alpha}\mu^{-1/6}\sqrt{r}\rho^{13/24}q_r^{91/120} \right),$$

where

$$r = \left(\frac{1.21 \cdot 10^{-5}}{q_r + e_3 \rho^{-3/4} q_r^{1/4}} \right)^{4/15} \quad \text{and} \quad \mu = \frac{1.458 \cdot 10^{-6} T^{3/2}}{T + 110.4}.$$

- *Autoconversion: Collision of cloud droplets, forming rain drops*

The growth of cloud droplets to larger sizes is dominated by collision processes. The collision of two cloud droplets leading to a larger rain drop is called autoconversion; see, e.g., [20]. This rate can be modeled as

$$A_1 = 10^{-3} k_1 \rho q_c^2.$$

Note that the coefficient k_1 cannot be measured or derived from the first principles. It is a free parameter, which must be fixed using parameter estimations. Thus, the impact of the uncertainty of this parameter is of high interest. In our deterministic experiments, we choose $k_1 = 0.0041$.

- *Accretion: Collection of cloud droplets by rain drops*

Falling rain drops can also collect smaller cloud droplets. This process is called accretion and can be modelled as

$$A_2 = 0.3846 k_2 \alpha r \rho^{1/4} q_c q_r^{61/60}.$$

Again, the parameters k_2 and α cannot be derived from the first principles and the impact of their uncertainty is of high interest as well. In our deterministic experiments, we chose $k_2 = 0.8$ and $\alpha = 190.3$.

- *Sedimentation of rain drops*

Large rain drops are accelerated by gravity force. Frictional forces balance gravity, thus we can assume that a rain drop falls with a terminal velocity, which depends only on the mass of the drop and the density of air. The terminal velocity is given by

$$v_q = \sqrt{1.225\alpha r \rho^{-1/2} q_r^{4/15}}.$$

We have to introduce an additional hyperbolic term into the equation for the evolution of q_r , that is, the term $\nabla \cdot (-v_q \rho q_r \mathbf{e}_3)$ is included.

Note that the condensation and evaporation processes are formulated explicitly, in contrast to the usual approach of saturation adjustment (see, e.g., [25]), which is less accurate, but commonly used in operational weather forecast models. This explicit formulation introduces stiffness caused by modeling cloud processes on the RHS of the cloud equations with fractional exponents between -1 and 1 . We handle this stiffness by replacing terms like ζ^ξ , $\xi \in (-1, 1)$, with

$$\begin{cases} \zeta^\xi, & \text{if } \zeta > 10^{-16}, \\ 0, & \text{otherwise.} \end{cases}$$

Due to the condensation and evaporation processes latent heat is released or absorbed. These processes are modelled by the source term in (2.1):

$$S_\theta = \rho \frac{L\theta}{c_p T} (C - E), \quad (2.6)$$

where $L = 2.53 \cdot 10^6$ [J/kg] is the specific latent heat of vaporization.

Solving the Navier-Stokes equations (2.1) in a weakly compressible regime is known to cause numerical instabilities due to the multiscale effects. We follow the approach typically used in meteorological models, where the dynamics of interest is described by a perturbation of a background state, which is the hydrostatic equilibrium. The latter expresses a balance between the gravity and pressure forces. Denoting by \bar{p} , $\bar{\rho}$, $\bar{\mathbf{u}} = 0$, $\bar{\theta}$ and $\bar{\rho\theta}$ the respective background state, the hydrostatic equilibrium satisfies

$$\frac{\partial \bar{p}}{\partial x_3} = -\bar{\rho}g, \quad S_\theta = 0,$$

where \bar{p} is obtained from the equation of state (2.4)

$$\bar{p} = p(\bar{\rho\theta}) = p_0 \left(\frac{R\bar{\rho\theta}}{p_0} \right)^{\gamma_m}. \quad (2.7)$$

Let p' , ρ' , \mathbf{u}' , θ' and $(\rho\theta)'$ stand for the corresponding perturbations of the equilibrium state, then

$$p = \bar{p} + p', \quad \rho = \bar{\rho} + \rho', \quad \theta = \bar{\theta} + \theta', \quad \mathbf{u} = \mathbf{u}', \quad \rho\theta = \bar{\rho\theta} + \bar{\rho}\theta' + \rho'\bar{\theta} + \rho'\theta' = \bar{\rho\theta} + (\rho\theta)'$$

The pressure perturbation p' is derived from (2.4) and (2.7) using the following Taylor expansion

$$p(\rho\theta) \approx p(\bar{\rho\theta}) + \frac{\partial p}{\partial(\rho\theta)} (\rho\theta - \bar{\rho\theta}) = \bar{p} + \gamma_m p_0 \left(\frac{R\bar{\rho\theta}}{p_0} \right)^{\gamma_m} \frac{(\rho\theta)'}{\bar{\rho\theta}},$$

which results in

$$p' \approx \gamma_m p_0 \left(\frac{R\bar{\rho\theta}}{p_0} \right)^{\gamma_m} \frac{(\rho\theta)'}{\bar{\rho\theta}}.$$

The perturbation formulation of the Navier-Stokes equations (2.1) then reads as

$$\begin{aligned} \rho'_t + \nabla \cdot (\rho\mathbf{u}) &= 0, \\ (\rho\mathbf{u})_t + \nabla \cdot (\rho\mathbf{u} \otimes \mathbf{u} + p' \text{Id} - \mu_m \rho (\nabla\mathbf{u} + (\nabla\mathbf{u})^\top)) &= -\rho' g \mathbf{e}_3, \\ (\rho\theta)'_t + \nabla \cdot (\rho\theta\mathbf{u} - \mu_h \rho \nabla\theta) &= S_\theta. \end{aligned} \quad (2.8)$$

Note that though the systems (2.8) and (2.1) are equivalent, the perturbation formulation (2.8) is preferable for the development of a numerical scheme. For alternative representations of cloud dynamics and their numerical investigations, we refer the reader to [3, 42] and references therein.

3. STOCHASTIC MATHEMATICAL MODEL

In the meteorological model described in Section 2, some data or parameters may contain uncertainty. In this paper, we consider the case, where the uncertainty arises from the initial data or some coefficients in the microphysical cloud parameterizations. In order to mathematically describe the uncertainty, we introduce a random variable ω . We assume that either the initial data or some well-chosen model parameters depend on ω , that is,

$$(\rho q_\ell)|_{t=0} = (\rho q_\ell)(\mathbf{x}, t = 0, \omega) \quad \text{with } \ell \in \{v, c, r\}$$

or

$$k_1 = k_1(\omega), \quad k_2 = k_2(\omega), \quad \alpha = \alpha(\omega).$$

Consequently, the solution at later time will also depend on ω , that is, $(\rho q_\ell)(\mathbf{x}, t, \omega)$ for $\ell \in \{v, c, r\}$, and the system (2.2) for cloud variables will read as

$$\begin{aligned} ((\rho q_v)(\omega))_t + \nabla \cdot ((\rho q_v)(\omega) \mathbf{u} - \mu_q \rho \nabla q_v(\omega)) &= \rho(-C(\omega) + E(\omega)), \\ ((\rho q_c)(\omega))_t + \nabla \cdot ((\rho q_c)(\omega) \mathbf{u} - \mu_q \rho \nabla q_c(\omega)) &= \rho(C(\omega) - A_1(\omega) - A_2(\omega)), \\ ((\rho q_r)(\omega))_t + \nabla \cdot ((\rho q_r)(\omega)(-v_q(\omega) \mathbf{e}_3 + \mathbf{u}) - \mu_q \rho \nabla q_r(\omega)) &= \rho(A_1(\omega) + A_2(\omega) - E(\omega)). \end{aligned} \quad (3.1)$$

From now on we will stress the dependence on ω , but we will omit the dependence on \mathbf{x} and t to simplify the notation. We would like to point out that the solution of the Navier-Stokes equations (2.8) will also depend on ω , because of the source term S_θ . In this paper, we will consider a simplified situation by replacing

$$S_\theta(\omega) = \rho \frac{L\theta}{c_p T} \{C((\rho q_v)(\omega), (\rho q_c)(\omega)) - E((\rho q_v)(\omega), (\rho q_r)(\omega))\}$$

in (2.8) by \bar{S}_θ which only depends on the expected values of the cloud variables

$$\bar{S}_\theta := \rho \frac{L\theta}{c_p T} \{C(\mathbb{E}[\rho q_v], \mathbb{E}[\rho q_c]) - E(\mathbb{E}[\rho q_v], \mathbb{E}[\rho q_r])\}.$$

This ensures that all of the fluid variables, ρ' , $\rho \mathbf{u}$ and $(\rho \theta)'$, remain deterministic.

4. NUMERICAL SCHEME FOR THE DETERMINISTIC MODEL

The numerical approximation of the coupled model (2.8), (2.2) is based on the second-order Strang operator splitting. Therefore, we split the whole system into the macroscopic Navier-Stokes flow equations and the microscopic cloud equations. The Navier-Stokes equations (2.8) are approximated by an IMEX finite-volume method and the cloud equations (2.2) are approximated by a finite-volume method in space and an explicit Runge-Kutta method with an enlarged stability region in time.

4.1. Operator form. Let $\mathbf{w} := (\rho', \rho \mathbf{u}, (\rho \theta)')^\top$ and $\mathbf{w}_q := (\rho q_v, \rho q_c, \rho q_r)^\top$ denote the solution vectors of (2.8) and (2.2), respectively. Then, the coupled system can be written as

$$\begin{aligned} \mathbf{w}_t &= -\nabla \cdot \mathbf{F}(\mathbf{w}) + \mathfrak{D}(\mathbf{w}) + \mathfrak{R}(\mathbf{w}), \\ (\mathbf{w}_q)_t &= -\nabla \cdot \mathbf{F}_q(\mathbf{w}_q) + \mathfrak{D}_q(\mathbf{w}_q) + \mathfrak{R}_q(\mathbf{w}_q), \end{aligned}$$

where \mathbf{F} and \mathbf{F}_q are advection fluxes and \mathfrak{D} , \mathfrak{R} and \mathfrak{D}_q , \mathfrak{R}_q denote the diffusion and reaction operators of the respective systems. They are given by

$$\begin{aligned} \mathbf{F}(\mathbf{w}) &:= (\rho \mathbf{u}, \rho \mathbf{u} \otimes \mathbf{u} + p' \text{Id}, \rho \theta \mathbf{u})^\top, \\ \mathfrak{D}(\mathbf{w}) &:= (0, \nabla \cdot (\mu_m \rho (\nabla \mathbf{u} + (\nabla \mathbf{u})^\top)), \nabla \cdot (\mu_h \rho \nabla \theta))^\top, \\ \mathfrak{R}(\mathbf{w}) &:= (0, -\rho' g \mathbf{e}_3, S_\theta)^\top, \\ \mathbf{F}_q(\mathbf{w}_q) &:= (\rho q_v \mathbf{u}, \rho q_c \mathbf{u}, \rho q_r \mathbf{u} - v_q \rho q_r \mathbf{e}_3)^\top, \\ \mathfrak{D}_q(\mathbf{w}_q) &:= (\nabla \cdot (\mu_q \rho \nabla q_v), \nabla \cdot (\mu_q \rho \nabla q_c), \nabla \cdot (\mu_q \rho \nabla q_r))^\top, \\ \mathfrak{R}_q(\mathbf{w}_q) &:= (-C + E, C - A_1 - A_2, A_1 + A_2 - E)^\top. \end{aligned} \quad (4.1)$$

In order to derive an asymptotically stable, accurate and computational efficient scheme for the Navier-Stokes equations, we first split the equations into linear and nonlinear parts; see [6, 27] and references therein. Consequently, we introduce

- $\mathbf{F}(\mathbf{w}) = \mathbf{F}_L(\mathbf{w}) + \mathbf{F}_N(\mathbf{w})$ with $\mathbf{F}_L(\mathbf{w}) := (\rho\mathbf{u}, p' \text{Id}, \bar{\theta}\rho\mathbf{u})^\top$ and $\mathbf{F}_N(\mathbf{w}) := (0, \rho\mathbf{u} \otimes \mathbf{u}, \theta'\rho\mathbf{u})^\top$;

- $\mathfrak{D}(\mathbf{w}) = \mathfrak{D}_L(\mathbf{w}) + \mathfrak{D}_N(\mathbf{w})$ with

$$\mathfrak{D}_L(\mathbf{w}) := (0, \mu_m(\Delta(\rho\mathbf{u}) + \nabla(\nabla \cdot (\rho\mathbf{u}))), \mu_h\Delta(\rho\theta)')^\top \text{ and}$$

$$\mathfrak{D}_N(\mathbf{w}) := (0, -\mu_m((\Delta\rho)\mathbf{u} + (D^2\rho)\mathbf{u} + \nabla\mathbf{u}\nabla\rho + \nabla\rho\nabla \cdot \mathbf{u}), \mu_h(\Delta(\bar{\rho}\theta) - \theta\Delta\rho - \nabla\rho \cdot \nabla\theta))^\top;$$

- $\mathfrak{R}(\mathbf{w}) = \mathfrak{R}_L(\mathbf{w}) + \mathfrak{R}_N(\mathbf{w})$ with $\mathfrak{R}_L(\mathbf{w}) := (0, -\rho'g\mathbf{e}_3, 0)^\top$ and $\mathfrak{R}_N(\mathbf{w}) := (0, 0, S_\theta)^\top$.

We would like to point out that the choice of the linear and nonlinear operators is crucial. We choose the linear part to model linear acoustic and gravitational waves as well as linear viscous fluxes. The nonlinear part describes nonlinear advective effects together with the remaining nonlinear viscous fluxes and the influence of the latent heat. We will use the following notation:

$$\mathcal{L} := -\nabla \cdot \mathbf{F}_L(\mathbf{w}) + \mathfrak{D}_L(\mathbf{w}) + \mathfrak{R}_L(\mathbf{w}) \quad \text{and} \quad \mathcal{N} := -\nabla \cdot \mathbf{F}_N(\mathbf{w}) + \mathfrak{D}_N(\mathbf{w}) + \mathfrak{R}_N(\mathbf{w}).$$

4.2. Discretization in space. The spatial discretization is realized by a finite-volume method. We take a cuboid computational domain $\Omega \subset \mathbb{R}^d$, which is divided into N uniform Cartesian cells. The cells are labelled in a certain order using a single-index notation. For simplicity of notation, we assume that the cells are cubes with the sides of size h so that $|C_i| = h^d$. We also introduce the notation $S(i)$ for the set of all neighbouring cells of cell C_i , $i = 1, \dots, N$.

We assume that at a certain time t the approximate solution is realized in terms of its cell averages

$$\mathbf{w}_i(t) \approx \frac{1}{h^d} \int_{C_i} \mathbf{w}(\mathbf{x}, t) \, d\mathbf{x} \quad \text{and} \quad (\mathbf{w}_q)_i(t) \approx \frac{1}{h^d} \int_{C_i} \mathbf{w}_q(\mathbf{x}, t) \, d\mathbf{x}, \quad i = 1, \dots, N.$$

In order to simplify the notation, we will now omit the time dependence of $\mathbf{w}_i(t)$ and $(\mathbf{w}_q)_i(t)$. Next, we introduce the notation $\mathbf{w}_h := \{\mathbf{w}_i\}_{i=1}^N$ and $(\mathbf{w}_q)_h := \{(\mathbf{w}_q)_i\}_{i=1}^N$ and consider the following approximation of the advection, diffusion and reaction operators:

$$\mathcal{A}_i(\mathbf{w}_h) = (\mathcal{A}_L)_i(\mathbf{w}_h) + (\mathcal{A}_N)_i(\mathbf{w}_h) \approx \frac{1}{h^d} \int_{C_i} \nabla \cdot \mathbf{F}_L(\mathbf{w}(\mathbf{x}, t)) \, d\mathbf{x} + \frac{1}{h^d} \int_{C_i} \nabla \cdot \mathbf{F}_N(\mathbf{w}(\mathbf{x}, t)) \, d\mathbf{x},$$

$$\mathcal{D}_i(\mathbf{w}_h) = (\mathcal{D}_L)_i(\mathbf{w}_h) + (\mathcal{D}_N)_i(\mathbf{w}_h) \approx \frac{1}{h^d} \int_{C_i} \mathfrak{D}_L(\mathbf{w}(\mathbf{x}, t)) \, d\mathbf{x} + \frac{1}{h^d} \int_{C_i} \mathfrak{D}_N(\mathbf{w}(\mathbf{x}, t)) \, d\mathbf{x},$$

$$\mathcal{R}_i(\mathbf{w}_h) = (\mathcal{R}_L)_i(\mathbf{w}_h) + (\mathcal{R}_N)_i(\mathbf{w}_h) \approx \frac{1}{h^d} \int_{C_i} \mathfrak{R}_L(\mathbf{w}(\mathbf{x}, t)) \, d\mathbf{x} + \frac{1}{h^d} \int_{C_i} \mathfrak{R}_N(\mathbf{w}(\mathbf{x}, t)) \, d\mathbf{x}.$$

Analogous notation will be used for the approximations $(\mathcal{A}_q)_i(\mathbf{w}_h)$, $(\mathcal{D}_q)_i(\mathbf{w}_h)$ and $(\mathcal{R}_q)_i(\mathbf{w}_h)$ of the cloud operators.

4.2.1. *Advection.* The advection terms are discretized using flux functions as follows:

$$\begin{aligned} (\mathcal{A}_L)_i(\mathbf{w}_h) &= \frac{1}{h} \sum_{j \in S(i)} H_{ij}^L(\mathbf{w}_h) \sum_{k=1}^d n_{ij}^{(k)}, \\ (\mathcal{A}_N)_i(\mathbf{w}_h) &= \frac{1}{h} \sum_{j \in S(i)} H_{ij}^N(\mathbf{w}_h) \sum_{k=1}^d n_{ij}^{(k)}, \\ (\mathcal{A}_q)_i((\mathbf{w}_q)_h) &= \frac{1}{h} \sum_{j \in S(i)} (H_q)_{ij}((\mathbf{w}_q)_h) \sum_{k=1}^d n_{ij}^{(k)}, \end{aligned}$$

where the numerical fluxes H_{ij}^L , H_{ij}^N and $(H_q)_{ij}$ approximate the corresponding fluxes between the computational cells C_i and C_j , and $n_{ij}^{(k)}$ denotes the k -th component of the outer normal unit vector of cell C_i in the direction of cell C_j . We use the Rusanov numerical flux for H_{ij}^N and $(H_q)_{ij}$ and the central flux for H_{ij}^L . For $(\mathcal{A}_N)_i(\mathbf{w}_h)$ and $(\mathcal{A}_q)_i((\mathbf{w}_q)_h)$ a second-order discretization is obtained via a MUSCL-type approach using piecewise linear reconstructions with the minmod limiter. The numerical fluxes are then given by

$$\begin{aligned} H_{ij}^L(\mathbf{w}_h) &= \frac{1}{2} (\mathbf{F}_L(\mathbf{w}_j) + \mathbf{F}_L(\mathbf{w}_i)), \\ H_{ij}^N(\mathbf{w}_h) &= \frac{1}{2} (\mathbf{F}_N(\mathbf{w}_{ij}^+) + \mathbf{F}_N(\mathbf{w}_{ij}^-)) - \frac{\lambda_{ij}}{2} (\mathbf{w}_{ij}^+ - \mathbf{w}_{ij}^-), \\ (H_q)_{ij}((\mathbf{w}_q)_h) &= \frac{1}{2} (\mathbf{F}_q((\mathbf{w}_q)_{ij}^+) + \mathbf{F}_q((\mathbf{w}_q)_{ij}^-)) - \frac{(\lambda_q)_{ij}}{2} ((\mathbf{w}_q)_{ij}^+ - (\mathbf{w}_q)_{ij}^-). \end{aligned} \quad (4.2)$$

Here, \mathbf{w}_{ij}^- , \mathbf{w}_{ij}^+ and $(\mathbf{w}_q)_{ij}^-$, $(\mathbf{w}_q)_{ij}^+$ denote the corresponding interface values, which are computed using a piecewise linear reconstruction so that

$$\mathbf{w}_{ij}^- = \mathbf{w}_i + \mathbf{s}_{ij} \frac{h}{2} \sum_{k=1}^d n_{ij}^{(k)}, \quad \mathbf{w}_{ij}^+ = \mathbf{w}_j - \mathbf{s}_{ji} \frac{h}{2} \sum_{k=1}^d n_{ij}^{(k)},$$

where the slopes \mathbf{s}_{ij} are computed by the mindmod limiter,

$$\mathbf{s}_{ij} = \frac{1}{h} \text{minmod}(\mathbf{w}_j - \mathbf{w}_i, \mathbf{w}_i - \mathbf{w}_{j^*}) \sum_{k=1}^d n_{ij}^{(k)},$$

applied in a component-wise manner. Here,

$$\text{minmod}(a, b) = \begin{cases} a, & \text{if } |a| < |b| \text{ and } ab > 0, \\ b, & \text{if } |b| < |a| \text{ and } ab > 0, \\ 0, & \text{if } ab \leq 0, \end{cases}$$

and $(\mathbf{w}_q)_{ij}^-$ and $(\mathbf{w}_q)_{ij}^+$ are obtained similarly. Thereby C_{j^*} is the other neighboring cell of C_i in the opposite direction from C_j . Finally, the values λ_{ij} and $(\lambda_q)_{ij}$ are given by

$$\lambda_{ij} = \max \left\{ \sigma \left(\frac{\partial \mathbf{F}_N(\mathbf{w}_{ij}^-)}{\partial \mathbf{w}} \right), \sigma \left(\frac{\partial \mathbf{F}_N(\mathbf{w}_{ij}^+)}{\partial \mathbf{w}} \right) \right\}, \quad (\lambda_q)_{ij} = \max \left\{ \sigma \left(\frac{\partial \mathbf{F}_q((\mathbf{w}_q)_{ij}^-)}{\partial \mathbf{w}_q} \right), \sigma \left(\frac{\partial \mathbf{F}_q((\mathbf{w}_q)_{ij}^+)}{\partial \mathbf{w}_q} \right) \right\},$$

where σ denotes the spectral radius of the corresponding Jacobians.

Remark 4.1. Note that in the computation of H_{ij}^L in (4.2), we use the cell averages rather than the point values at the cell interfaces for the following two reasons. First, the flux is second-order accurate. Second, in Section 4.3, we will treat the linear part of the flux implicitly and this is much easier to do when the numerical flux is linear as well.

4.2.2. *Diffusion.* The components of the discrete diffusion operators are discretized in a straightforward manner using second-order central differences.

4.2.3. *Reaction.* The reaction terms are discretized by a direct evaluation of the reaction operators at the cell centres:

$$\mathcal{R}_i(\mathbf{w}_h) = \mathfrak{R}_L(\mathbf{w}_i) + \mathfrak{R}_N(\mathbf{w}_i), \quad (\mathcal{R}_q)_i((\mathbf{w}_q)_h) = \mathfrak{R}_q((\mathbf{w}_q)_i).$$

After the spatial discretization, we obtain the following system of time-dependent ODEs:

$$\frac{d}{dt} \mathbf{w}_i = -\mathcal{A}_i(\mathbf{w}_h) + \mathcal{D}_i(\mathbf{w}_h) + \mathcal{R}_i(\mathbf{w}_h), \quad (4.3)$$

$$\frac{d}{dt} (\mathbf{w}_q)_i = -(\mathcal{A}_q)_i((\mathbf{w}_q)_h) + (\mathcal{D}_q)_i((\mathbf{w}_q)_h) + (\mathcal{R}_q)_i((\mathbf{w}_q)_h). \quad (4.4)$$

This system has to be solved using an appropriate ODE solver as discussed in Section 4.3.

4.3. Discretization in time. Let \mathbf{w}_h^n and $(\mathbf{w}_q)_h^n$ denote the numerical approximation of the solutions $\mathbf{w}_h(t)$ and $(\mathbf{w}_q)_h(t)$ at the discrete time level t^n . We evolve the solution to the next time level $t^{n+1} = t^n + \Delta t^n$, where Δt^n is the size of the Strang operator splitting time step. In the operator splitting approach, we first numerically solve the ODE system (4.3) with $\Delta t_{\text{NS}}^n = \Delta t^n/2$, we then numerically integrate the ODE system (4.4) with Δt^n and finally we solve the system (4.3) again with Δt_{NS}^n .

Notice that the system (4.3) may be very stiff as the Navier-Stokes equations are in the weakly compressible regime. We therefore follow the approach in [6] (see also [5]), and employ the second-order ARS(2,2,2) IMEX method from [2]:

$$\begin{aligned} \mathbf{w}_h^{n+\frac{1}{4}} &= \mathbf{w}_h^n + \beta \Delta t_{\text{NS}}^n \left(\mathcal{L} \left(\mathbf{w}_h^{n+\frac{1}{4}} \right) + \mathcal{N} \left(\mathbf{w}_h^n \right) \right), \\ \mathbf{w}_h^{n+\frac{1}{2}} &= \mathbf{w}_h^n + \Delta t_{\text{NS}}^n \left(\delta \mathcal{N} \left(\mathbf{w}_h^n \right) + (1 - \delta) \mathcal{N} \left(\mathbf{w}_h^{n+\frac{1}{4}} \right) \right) + \Delta t_{\text{NS}}^n \left(\beta \mathcal{L} \left(\mathbf{w}_h^{n+\frac{1}{2}} \right) + (1 - \beta) \mathcal{L} \left(\mathbf{w}_h^{n+\frac{1}{4}} \right) \right), \end{aligned} \quad (4.5)$$

where $\alpha = 1 - 1/\sqrt{2}$, $\delta = 1 - 1/2\beta$, $t^{n+\frac{1}{2}} = t^n + \Delta t_{\text{NS}}^n$, $t^{n+\frac{1}{4}} = t^n + \Delta t_{\text{NS}}^n/2$, and Δt_{NS}^n satisfies the following CFL condition:

$$\max_{s=1,2,3} \max_{i=1,\dots,N} (|(u_s)_i|) \frac{\Delta t_{\text{NS}}^n}{h} < 0.5.$$

For solving the linear systems arising in (4.5), we use the generalized minimal residual (GMRES) method combined with a preconditioner, the incomplete LU factorization (ILU). As it was shown in [6] (see also [5]), the resulting method is both accurate and efficient in the weakly compressible regime.

The ODE system (4.4) is also stiff, but its stiffness only comes from the diffusion and power-law-type source terms. We therefore efficiently solve it using the large stability domain third-order Runge-Kutta method from [32]. We have utilized the ODE solver DUMKA3, which is a free software that can be found in [31]. We note that DUMKA3 selects time steps automatically, but in order to improve its efficiency, one needs to provide the code with a time step stability restriction for the forward Euler method; see [31, 32]. This bound is obtained by $\min\{\Delta t^n, \Delta t_{\text{cloud}}^n\}$, where $\Delta t_{\text{cloud}}^n$ satisfies the following CFL condition for the cloud system:

$$\max_{s=1,2,3} \max_{i=1,\dots,N} (|(u_s)_i|, |v_q|) \frac{\Delta t_{\text{cloud}}^n}{h} < 0.5.$$

5. NUMERICAL SCHEME FOR THE STOCHASTIC MODEL

In this section, we describe a generalized polynomial chaos stochastic Galerkin (gPC-SG) method for the system of cloud equations (3.1). Such method belongs to the class of intrusive methods and the use of the Galerkin expansion leads to a system of deterministic equations for the expansion coefficients. In the gPC-SG method, the solution is sought in the form of a polynomial expansion

$$\rho q_\ell(\mathbf{x}, t, \omega) = \sum_{k=0}^M (\widehat{\rho q_\ell})_k(\mathbf{x}, t) \Phi_k(\omega) \quad \text{with } \ell \in \{v, c, r\}, M \geq 0, \quad (5.1)$$

where $\Phi_k(\omega)$, $k = 0, \dots, M$, are polynomials of k -th degree that are orthogonal with respect to the probability density function $\mu(\omega)$. More precisely, the polynomials satisfy

$$\int_{\Gamma} \Phi_k(\omega) \Phi_{k'}(\omega) \mu(\omega) d\omega = \delta_{kk'} \quad \text{for } 0 \leq k, k' \leq M, \quad (5.2)$$

where $\delta_{kk'}$ is the Kronecker symbol and Γ is the sample space. The choice of the orthogonal polynomials $\{\Phi_k(\omega)\}_{k=0}^M$ depends on the distribution of ω . In our case, we use a uniformly distributed $\omega \in \Gamma = (-1, 1)$, which defines the Legendre polynomials. We use the same expansion for the uncertain coefficients,

$$k_1(\omega) = \sum_{k=0}^M (\widehat{k}_1)_k \Phi_k(\omega), \quad k_2(\omega) = \sum_{k=0}^M (\widehat{k}_2)_k \Phi_k(\omega), \quad \alpha(\omega) = \sum_{k=0}^M \widehat{\alpha}_k \Phi_k(\omega), \quad (5.3)$$

for the source terms on the RHS of (3.1),

$$\begin{aligned} \rho(-C(\mathbf{x}, t, \omega) + E(\mathbf{x}, t, \omega)) &=: R_1(\mathbf{x}, t, \omega) = \sum_{k=0}^M (\widehat{r}_1)_k(\mathbf{x}, t) \Phi_k(\omega), \\ \rho(C(\mathbf{x}, t, \omega) - A_1(\mathbf{x}, t, \omega) - A_2(\mathbf{x}, t, \omega)) &=: R_2(\mathbf{x}, t, \omega) = \sum_{k=0}^M (\widehat{r}_2)_k(\mathbf{x}, t) \Phi_k(\omega), \\ \rho(A_1(\mathbf{x}, t, \omega) + A_2(\mathbf{x}, t, \omega) - E(\mathbf{x}, t, \omega)) &=: R_3(\mathbf{x}, t, \omega) = \sum_{k=0}^M (\widehat{r}_3)_k(\mathbf{x}, t) \Phi_k(\omega), \end{aligned} \quad (5.4)$$

as well as for the raindrop fall velocity,

$$v_q(\mathbf{x}, t, \omega) = \sum_{k=0}^M (\widehat{v}_q)_k(\mathbf{x}, t) \Phi_k(\omega). \quad (5.5)$$

Since $\rho(\mathbf{x}, t) = \widehat{\rho}_0(\mathbf{x}, t)$, we also obtain

$$q_\ell(\mathbf{x}, t, \omega) = \sum_{k=0}^M (\widehat{q}_\ell)_k(\mathbf{x}, t) \Phi_k(\omega) \quad \text{with} \quad (\widehat{q}_\ell)_k(\mathbf{x}, t) = \frac{(\widehat{\rho q}_\ell)_k(\mathbf{x}, t)}{\rho(\mathbf{x}, t)} \quad \text{for } \ell \in \{v, c, r\}, \quad k = 1, \dots, M. \quad (5.6)$$

We note that if $\rho(\mathbf{x}, t)$ is very small, the computation of the coefficients $(\widehat{q}_\ell)_k(\mathbf{x}, t)$ should be desingularized; see, e.g., [24], where several desingularization strategies were discussed.

Applying the Galerkin projection to (3.1) yields

$$\begin{aligned} \langle (\rho q_v)_t + \nabla \cdot (\rho q_v \mathbf{u} - \mu_q \rho \nabla q_v), \Phi_k \rangle &= \langle \rho(-C + E), \Phi_k \rangle, \\ \langle (\rho q_c)_t + \nabla \cdot (\rho q_c \mathbf{u} - \mu_q \rho \nabla q_c), \Phi_k \rangle &= \langle \rho(C - A_1 - A_2), \Phi_k \rangle, \\ \langle (\rho q_r)_t + \nabla \cdot (\rho q_r(-v_q \mathbf{e}_3 + \mathbf{u}) - \mu_q \rho \nabla q_r), \Phi_k \rangle &= \langle \rho(A_1 + A_2 - E), \Phi_k \rangle, \end{aligned} \quad (5.7)$$

for $k = 0, \dots, M$, where $\langle \cdot, \cdot \rangle$ is the scalar product in our probability space which is given through

$$\langle u, v \rangle = \int_{-1}^1 u(\omega) v(\omega) \mu(\omega) d\omega.$$

We now substitute (5.1), (5.4)–(5.6) into (5.7) and use the orthogonality property (5.2) to obtain the following $3(M+1) \times 3(M+1)$ deterministic system for the gPC coefficients:

$$\begin{aligned} \frac{\partial}{\partial t}(\widehat{\rho q_v})_k + \sum_{s=1}^d \frac{\partial}{\partial x_s} ((\widehat{\rho q_v})_k u_s) - \mu_q \sum_{s=1}^d \left(\frac{\partial \rho}{\partial x_s} \frac{\partial}{\partial x_s} (\widehat{q_v})_k + \rho \frac{\partial^2}{\partial x_s^2} (\widehat{q_v})_k \right) &= (\widehat{r_1})_k, \\ \frac{\partial}{\partial t}(\widehat{\rho q_c})_k + \sum_{s=1}^d \frac{\partial}{\partial x_s} ((\widehat{\rho q_c})_k u_s) - \mu_q \sum_{s=1}^d \left(\frac{\partial \rho}{\partial x_s} \frac{\partial}{\partial x_s} (\widehat{q_c})_k + \rho \frac{\partial^2}{\partial x_s^2} (\widehat{q_c})_k \right) &= (\widehat{r_2})_k, \\ \frac{\partial}{\partial t}(\widehat{\rho q_r})_k - \frac{\partial}{\partial x_d} \widehat{\alpha}_k + \sum_{s=1}^d \frac{\partial}{\partial x_s} ((\widehat{\rho q_r})_k u_s) - \mu_q \sum_{s=1}^d \left(\frac{\partial \rho}{\partial x_s} \frac{\partial}{\partial x_s} (\widehat{q_r})_k + \rho \frac{\partial^2}{\partial x_s^2} (\widehat{q_r})_k \right) &= (\widehat{r_3})_k, \end{aligned} \quad (5.8)$$

for $k = 0, \dots, M$. Here, the coefficients $\{\widehat{\alpha}_k\}_{k=0}^M$ are obtained using the following expansion:

$$v_q(\mathbf{x}, t, \omega)(\rho q_r)(\mathbf{x}, t, \omega) = \sum_{j=0}^M (\widehat{v}_q)_j(\mathbf{x}, t) \Phi_j(\omega) \sum_{m=0}^M (\widehat{\rho q_r})_m(\mathbf{x}, t) \Phi_m(\omega) =: \sum_{k=0}^M \widehat{\alpha}_k(\mathbf{x}, t) \Phi_k(\omega).$$

The coefficients $\{(\widehat{r_1})_k, (\widehat{r_2})_k, (\widehat{r_3})_k\}_{k=0}^M$, as well as $\{\widehat{\alpha}_k\}_{k=0}^M$ are calculated via discrete Legendre transform (DLT) and inverse discrete Legendre transform (IDLTL), which can be briefly described as follows.

- DLT: First, the Galerkin projection applied to the expansion $f(\mathbf{x}, t, \omega) = \sum_{k=0}^M \widehat{f}_k(\mathbf{x}, t) \Phi_k(\omega)$ yields

$$\widehat{f}_k(\mathbf{x}, t) = \frac{2k+1}{2} \int_{-1}^1 f(\mathbf{x}, t, \omega) \Phi_k(\omega) d\omega \quad \text{for } 0 \leq k \leq M. \quad (5.9)$$

Then, approximating the integral in (5.9) using the Gauss-Legendre quadrature leads to

$$\text{DLT} \left[\{f(\mathbf{x}, t, \omega_l)\}_{l=0}^M \right] = \left\{ \widehat{f}_k(\mathbf{x}, t) \right\}_{k=0}^M = \left\{ \frac{2k+1}{2} \sum_{l=0}^M \beta_l f(\mathbf{x}, t, \omega_l) \Phi_k(\omega_l) \right\}_{k=0}^M,$$

where β_l are the Gauss-Legendre quadrature weights and ω_l is the l -th root of Φ_{M+1} .

- IDLT: Given the coefficients $\{\widehat{f}_k\}_{k=0}^M$, we compute the function f through the gPC expansion

$$\text{IDLTL} \left[\left\{ \widehat{f}_k(\mathbf{x}, t) \right\}_{k=0}^M \right] = \{f(\mathbf{x}, t, \omega_l)\}_{l=0}^M = \left\{ \sum_{k=0}^M \widehat{f}_k(\mathbf{x}, t) \Phi_k(\omega_l) \right\}_{l=0}^M.$$

Consequently, we obtain

$$\{(\widehat{r_1})_k\}_{k=0}^M = \text{DLT} \left[R_1 \left(\text{IDLTL} \left[\{(\widehat{\rho q_v})_k\}_{k=0}^M \right], \text{IDLTL} \left[\{(\widehat{\rho q_c})_k\}_{k=0}^M \right], \text{IDLTL} \left[\{(\widehat{\rho q_r})_k\}_{k=0}^M \right] \right) \right],$$

and analogously for $\{(\widehat{r_2})_k\}_{k=0}^M$, $\{(\widehat{r_3})_k\}_{k=0}^M$ and $\{\widehat{\alpha}_k\}_{k=0}^M$.

Remark 5.1. We stress that since the values $\Phi_k(\omega_l)$, $0 \leq k, l \leq M$, are needed every time either DLT or IDLT is applied, one can precompute them for the code efficiency.

For the spatial and temporal discretizations of the system (5.8), we apply the same finite-volume method as described in Section 4.2 and the same large stability domain explicit time integration method mentioned in Section 4.3. As in the deterministic case, we implement the ODE solver DUMKA3, which we provide with the following time step stability restriction for the forward Euler method:

$$\max_{s=1,2,3} \max_{i=1,\dots,N} (|(u_s)_i|, |v_q(\omega_l)|) \frac{\Delta t_{\text{cloud}}^n}{h} < 0.5,$$

which should be satisfied for all of the Legendre roots ω_l , $l = 1, \dots, M$.

6. DETERMINISTIC NUMERICAL EXPERIMENTS

In this section, we test the numerical method described in Section 4. The experimental order of convergence is computed for the so-called free convection of a moist warm air bubble and the structure formation in cloud dynamics is shown in the Rayleigh-Bénard convection. The latter will be simulated in both the 2-D and 3-D cases.

6.1. Free convection of a moist warm air bubble in 2-D. We start with the well-known meteorological benchmark describing the free convection of a smooth warm air bubble; see, e.g., [7, 10].

Example 1: In this experiment, the warm bubble rises and deforms axisymmetrically due to the shear friction with the surrounding air at the warm/cold air interface, gradually forming a mushroom-like shape. The warm air bubble is placed at $(3500 [m], 2000 [m])$ with the initial perturbation

$$\begin{aligned} \rho'(\mathbf{x}, 0) &= -\bar{\rho}(\mathbf{x}) \frac{\theta'(\mathbf{x}, 0)}{\bar{\theta}(\mathbf{x}) + \theta'(\mathbf{x}, 0)}, \quad \bar{\rho}(\mathbf{x}) = \frac{p_0}{R\bar{\theta}(\mathbf{x})} \pi_e(\mathbf{x})^{\frac{1}{\gamma-1}}, \quad \pi_e(\mathbf{x}) = 1 - \frac{g x_3}{c_p \bar{\theta}}, \\ \mathbf{u}(\mathbf{x}, 0) &= 0, \\ \theta'(\mathbf{x}, 0) &= \begin{cases} 2 \cos^2\left(\frac{\pi r}{2}\right), & r := \sqrt{(x_1 - 3500)^2 + (x_3 - 2000)^2} \leq 2000, \\ 0, & \text{otherwise,} \end{cases} \end{aligned}$$

where $\bar{\theta} = 300 [K]$ and $p_0 = \bar{p} = 10^5 [Pa]$. The experiment was simulated in a domain $\Omega = [0, 7000] \times [0, 5000] [m^2]$. As initial conditions for the cloud variables we choose

$$q_v(\mathbf{x}, 0) = 0.02 \theta'(\mathbf{x}, 0), \quad q_c = 0, \quad q_r = 0.$$

We apply the no-flux boundary conditions $\mathbf{u} \cdot \mathbf{n} = 0$, $\nabla \rho' \cdot \mathbf{n} = 0$, $\nabla(\rho\theta)' \cdot \mathbf{n} = 0$, $\nabla(\rho q_\ell) \cdot \mathbf{n} = 0$, $\ell \in \{v, c, r\}$.

The experimental convergence study for the cloud and flow variables is presented in Tables 1 and 2, respectively. The experimental order of convergence has been computed in the following way:

$$EOC = \log_2 \left(\frac{\|v_{N, \Delta t} - v_{2N, \Delta t/2}\|_{L^1(\Omega)}}{\|v_{2N, \Delta t/2} - v_{4N, \Delta t/4}\|_{L^1(\Omega)}} \right),$$

where $v_{N, \Delta t}$ is the numerical solution computed on a grid with $N \times N$ grid cells and using a fixed time step Δt . As one can clearly see, the expected second order of accuracy has been achieved.

N	L^1 -error in ρq_v	EOC	L^1 -error in ρq_c	EOC	L^1 -error in ρq_r	EOC
10	3.594e+03	–	2.032e+01	–	1.096e+03	–
20	9.062e+02	1.99	5.407e+00	1.91	1.590e-07	32.68
40	2.624e+02	1.79	1.708e+00	1.66	4.856e-08	1.71
80	7.363e+01	1.83	5.159e-01	1.73	1.357e-08	1.84
160	1.989e+01	1.89	1.529e-01	1.75	3.564e-09	1.93

TABLE 1. *Example 1:* L^1 -errors and the corresponding EOCs for the cloud variables computed at the final time $t = 100s$ using $\Delta t = 20/N$.

6.2. Rayleigh-Bénard convection. In this experiment, we study a natural convection that is used to model structure formation. It occurs in a planar flow between two horizontal plates, where the lower one is heated from below and the upper one is cooled from above. Due to the presence of buoyancy, and hence gravity, the fluid develops a regular pattern of convection roles, known as the Bénard cells. In 3-D, these convection roles form additionally hexagonal structures; see, e.g., [1, 13, 37].

N	L^1 -error in ρ'	EOC	L^1 -error in ρu_1	EOC	L^1 -error in ρu_2	EOC	L^1 -error in $(\rho\theta)'$	EOC
10	1.050e+04	–	1.386e+06	–	1.671e+06	–	2.909e+06	–
20	1.207e+03	3.12	3.461e+05	2.00	3.005e+05	2.48	3.157e+05	3.20
40	2.900e+02	2.06	1.195e+05	1.53	9.923e+04	1.60	7.372e+04	2.10
80	9.282e+01	1.64	3.115e+04	1.94	2.894e+04	1.78	2.565e+04	1.52
160	2.528e+01	1.88	9.010e+03	1.79	8.406e+03	1.78	7.178e+03	1.84

TABLE 2. *Example 1: L^1 -errors and the corresponding EOCs for the flow variables computed at the final time $t = 100s$ using $\Delta t = 20/N$.*

For our numerical simulations, we prescribe the following initial conditions:

$$\rho'(\mathbf{x}, 0) = -\bar{\rho}(\mathbf{x}) \frac{\theta'(\mathbf{x}, 0)}{\bar{\theta}(\mathbf{x}) + \theta'(\mathbf{x}, 0)}, \quad \bar{\rho}(\mathbf{x}) = \frac{p_0}{R\bar{\theta}(\mathbf{x})} \pi_c(\mathbf{x})^{\frac{1}{\gamma-1}}, \quad \pi_c(\mathbf{x}) = 1 - \frac{gx_3}{c_p\bar{\theta}},$$

$$\mathbf{u}(\mathbf{x}, 0) = 0,$$

$$\theta'(\mathbf{x}, 0) = \eta(\mathbf{x}), \quad \bar{\theta}(\mathbf{x}) = 284 - \frac{1}{1000}x_3,$$

where $p_0 = \bar{p} = 10^5 [Pa]$ and $\eta(\mathbf{x})$ is a random perturbation uniformly distributed in $[-0.0021, 0.0021]$. For the cloud equations, the following initial data are used:

$$q_v(\mathbf{x}, 0) = 2 \cdot 10^{-5} \bar{\theta}(\mathbf{x}), \quad q_c = 0, \quad q_r = 0.$$

We apply periodic boundary conditions in horizontal direction and the following conditions vertically: $\mathbf{u} \cdot \mathbf{n} = 0$, $\nabla \rho' \cdot \mathbf{n} = 0$, $\nabla(\rho q_\ell) \cdot \mathbf{n} = 0$, $\ell \in \{v, c, r\}$ with the Dirichlet boundary conditions for the potential temperature,

$$\theta(x_3 = 0) = 284 [K] \quad \text{and} \quad \theta(x_3 = 1000) = 283 [K].$$

Example 2: 2-D case. In Figures 1–4, we present time snapshots of the numerical solution computed in a domain $\Omega = [0, 5000] \times [0, 1000] [m^2]$ that has been discretized using 320×320 mesh cells. In the beginning of the time evolution, usual finger-like structures are formed and rise to the top plate due to thermal conductivity. For dry air typical circular convection cells will be developed at a later time. In the case of moist air, the structures are less stable as one can see in Figure 1, where we plot the potential temperature θ computed at times $t = 1600, 2200$ and $2800s$. In Figure 2, the time evolution of water vapor q_v is depicted. Starting from many small structures, the circular-like roles are developed also for water vapor q_v and cloud drops q_c , see Figure 2 and 3, respectively. In Figure 4, we plot the rain q_r and can clearly recognize separate rain regions appearing at later times.

Example 3: 3-D case. In this example, we compute the numerical solution in a domain $\Omega = [0, 5000] \times [0, 5000] \times [0, 1000] [m^3]$ that has been discretized using $50 \times 50 \times 50$ mesh cells. In Figures 5–8, we show the computed solution at times $t = 1600, 2200, 2800$ and $3600s$. As one can clearly see, the expected hexagonal structures are formed. In order to visualize these structures, which can in particular been seen in the potential temperature (see Figure 5), we have plotted the solution in a slightly smaller domain $[0, 5000] \times [0, 5000] \times [0, 970] [m^3]$.

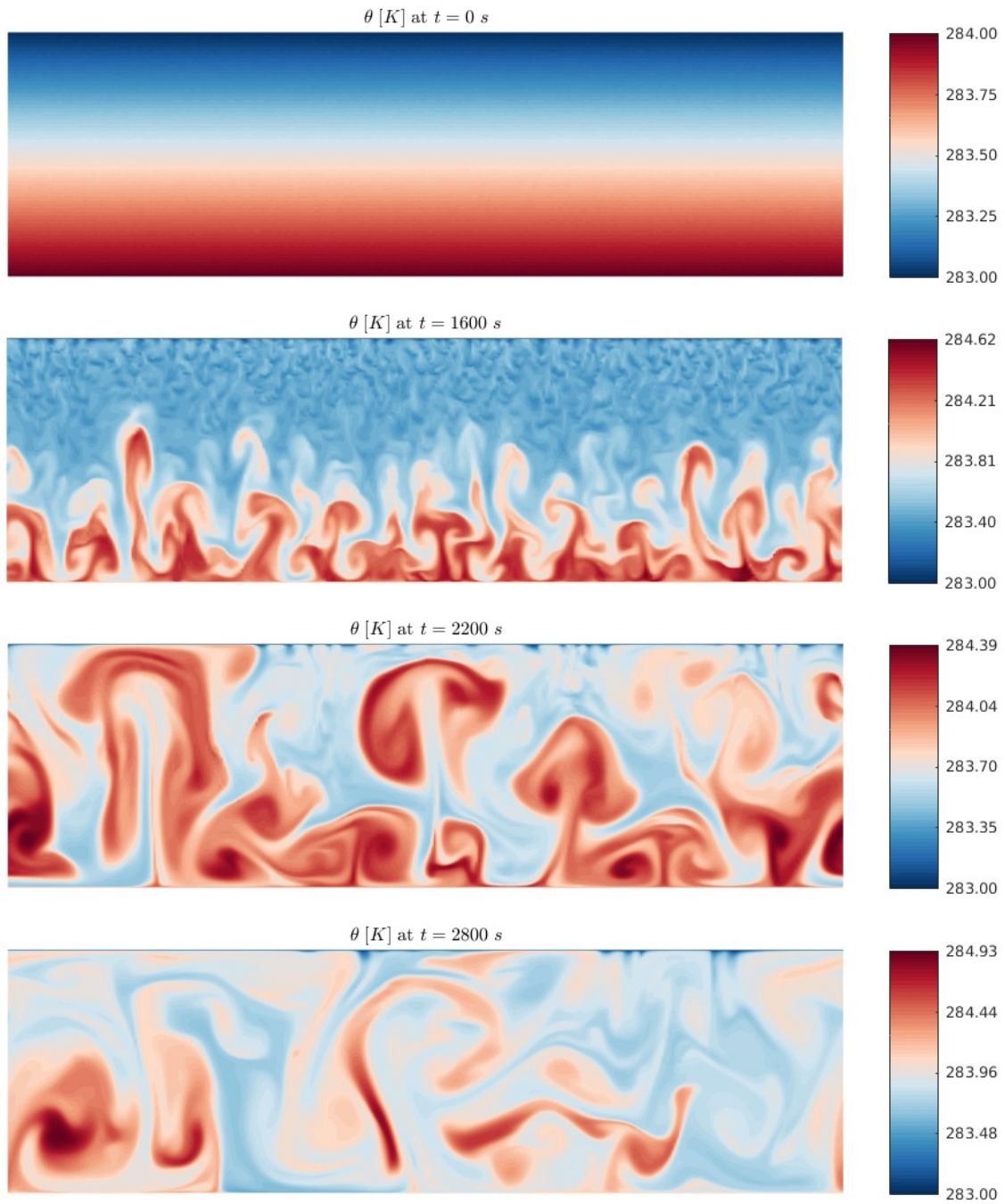


FIGURE 1. *Example 2: Time evolution of the potential temperature θ .*

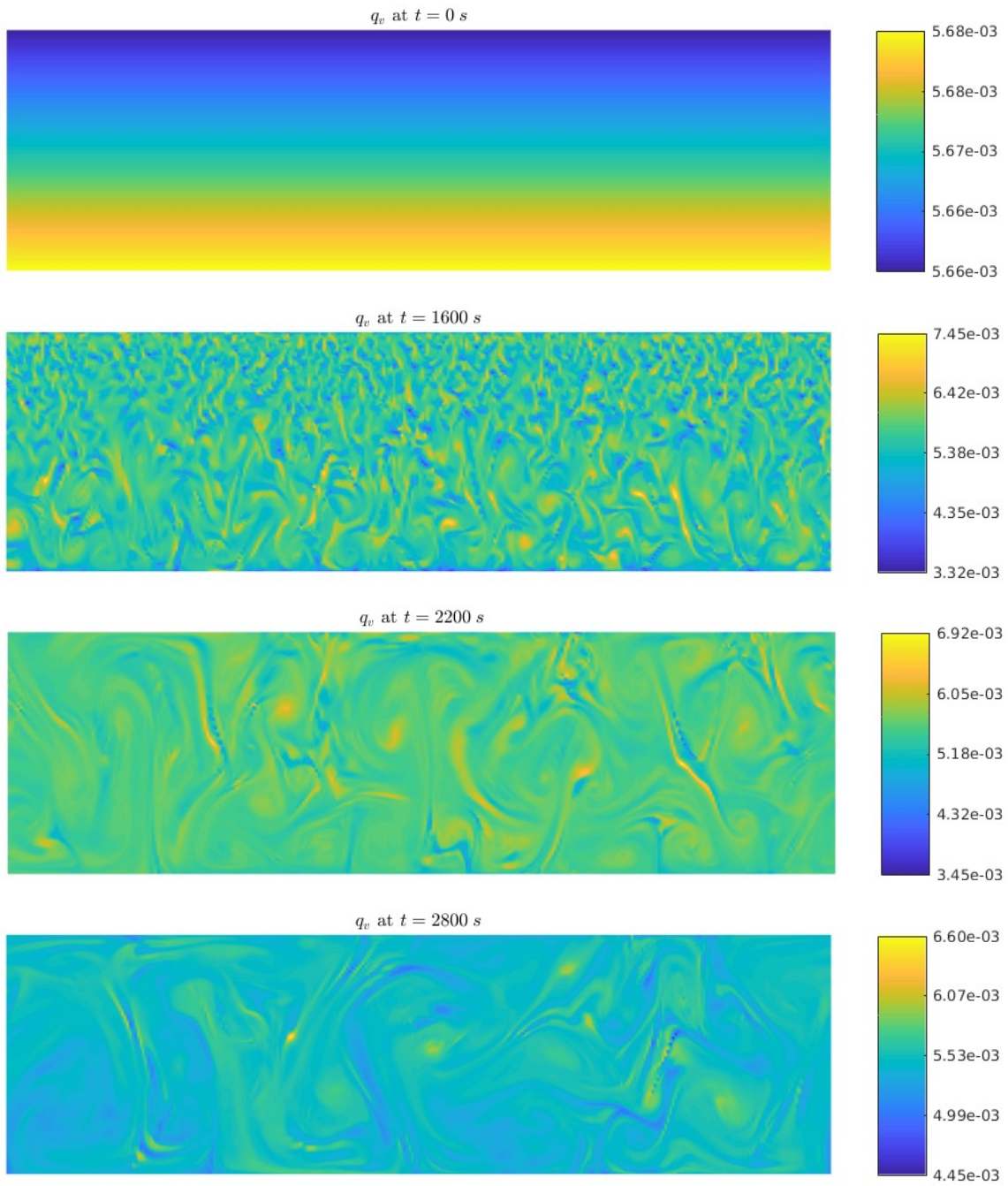


FIGURE 2. *Example 2: Time evolution of the water vapor concentration q_v .*

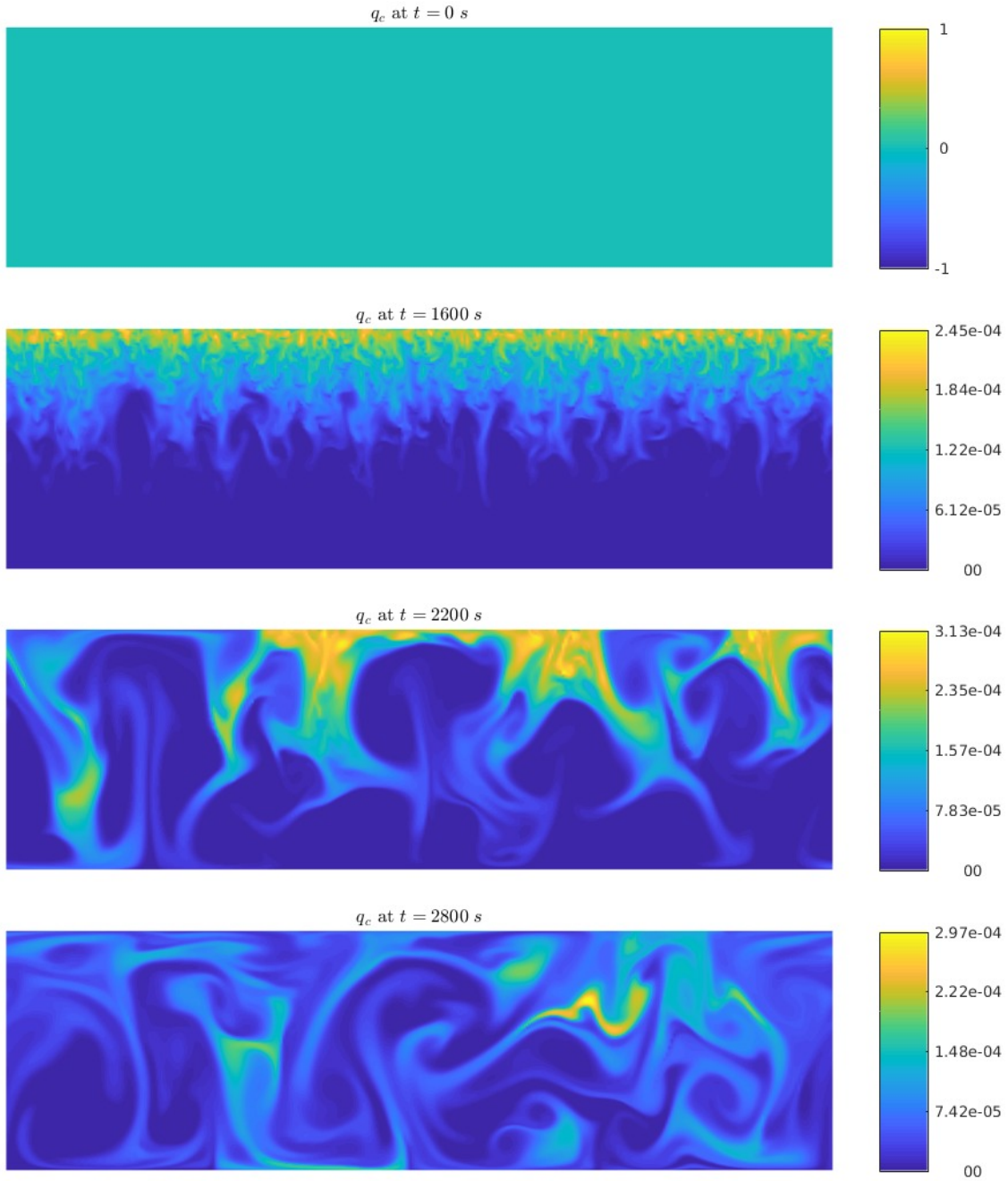


FIGURE 3. *Example 2: Time evolution of the cloud drops concentration q_c .*

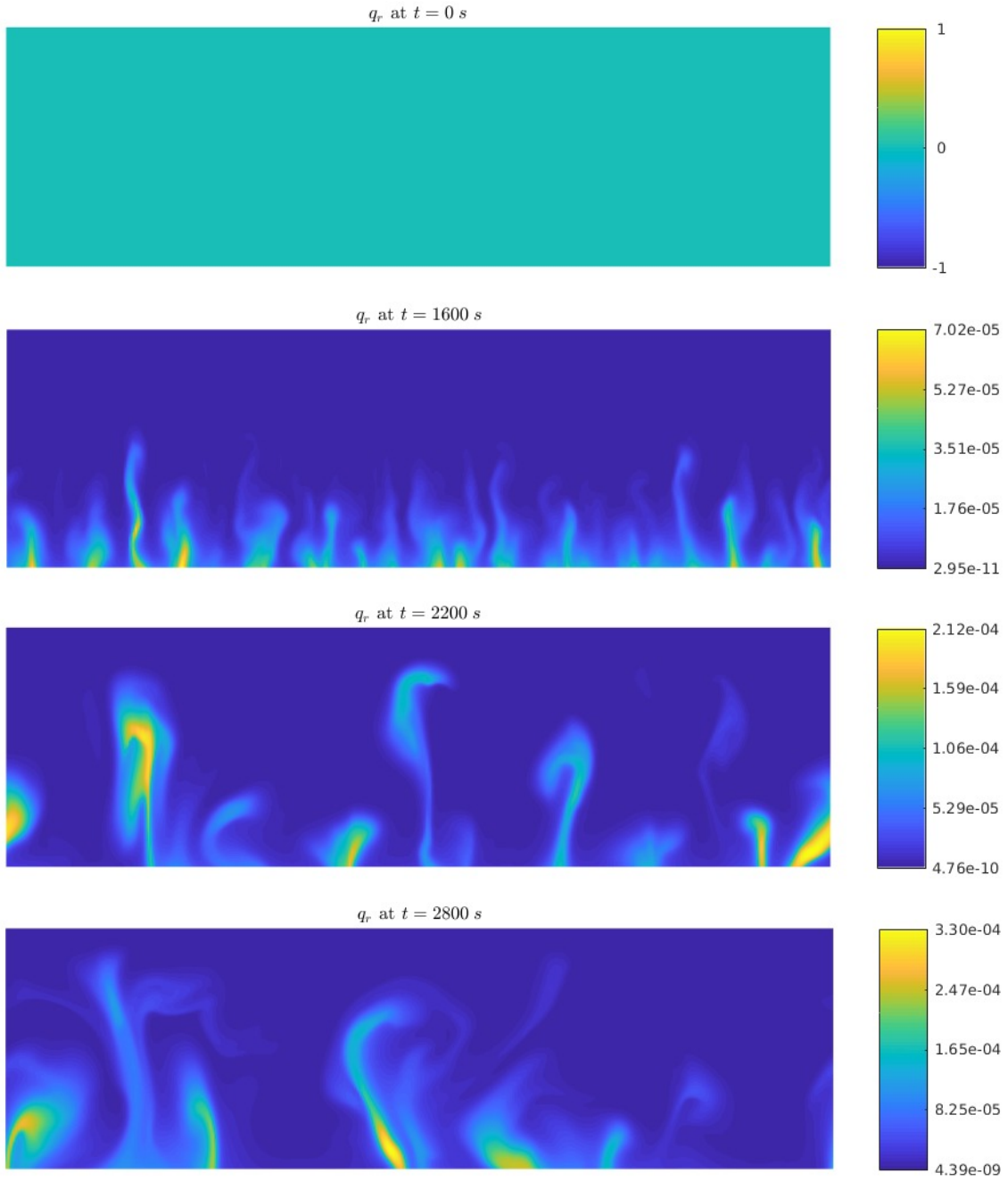


FIGURE 4. *Example 2: Time evolution of the rain concentration q_r .*

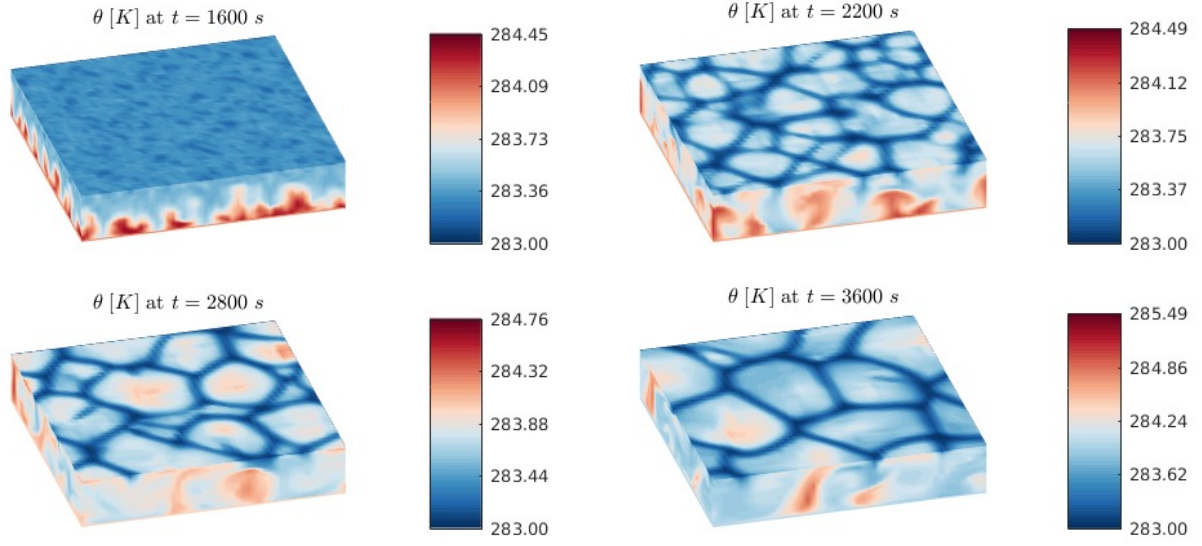


FIGURE 5. *Example 3: Time evolution of the potential temperature θ .*

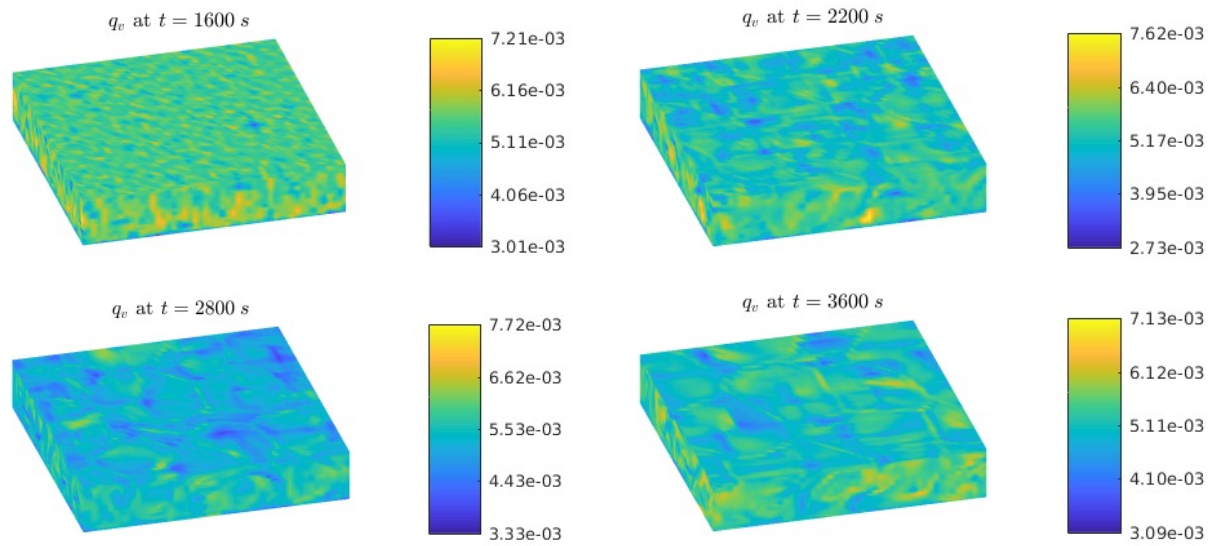


FIGURE 6. *Example 3: Time evolution of the water vapor concentration q_v .*

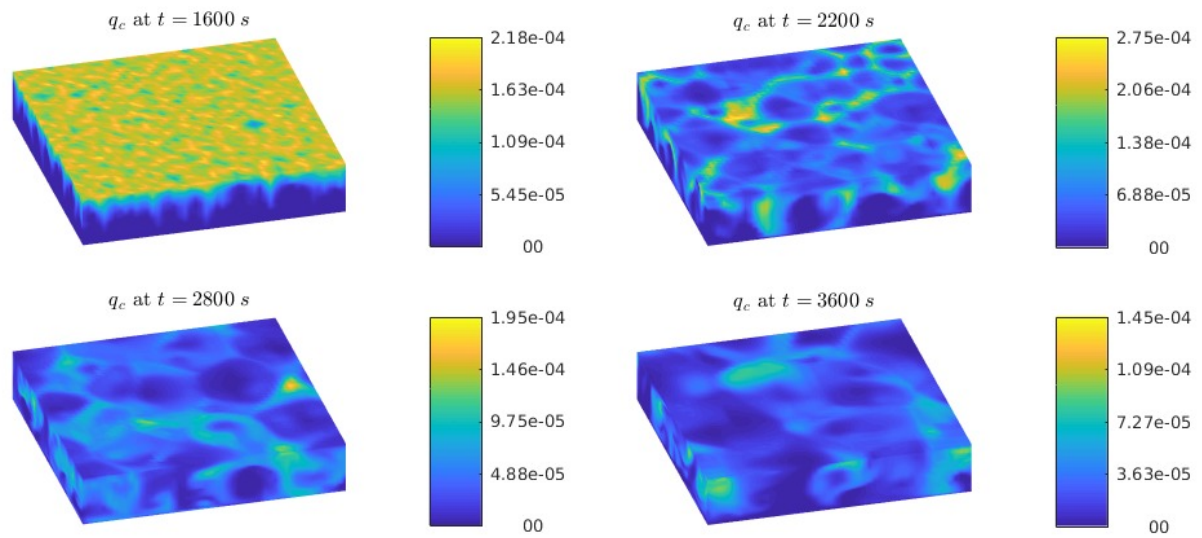


FIGURE 7. Example 3: Time evolution of the cloud drops concentration q_c .

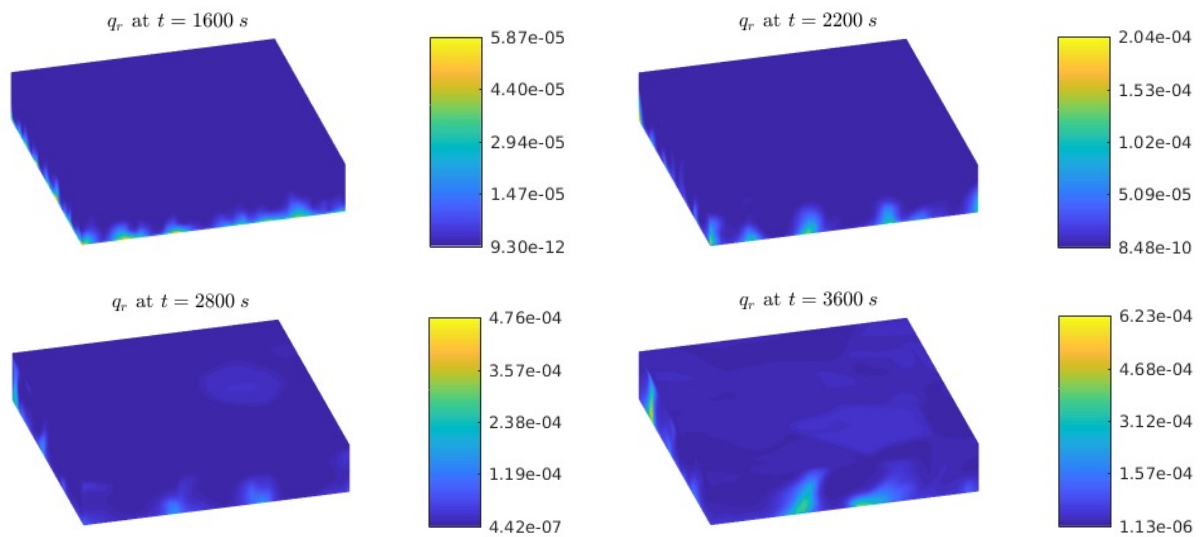


FIGURE 8. Example 3: Time evolution of the rain concentration q_r .

7. STOCHASTIC NUMERICAL EXPERIMENTS

In this section, we conduct numerical experiments with the stochastic Galerkin method described in Section 5 for the free convection of a moist warm air bubble and the Rayleigh-Bénard convection. We demonstrate the influence of uncertainty in initial data as well as in cloud parameters on the solution of the coupled Navier-Stokes-cloud model (2.8), (3.1). In all our numerical examples below we take $M = 3$.

7.1. Free convection of a smooth warm air bubble in 2-D. In this accuracy test, we modify Example 1 by perturbing the initial data.

Example 4: Stochastic initial data. We begin by considering the following stochastically perturbed initial data for the cloud variables:

$$\begin{aligned} (\widehat{q}_v)_0(\mathbf{x}, 0) &= 0.02\theta'(\mathbf{x}, 0), \quad (\widehat{q}_v)_1(\mathbf{x}, 0) = 0.1(\widehat{q}_v)_0(\mathbf{x}, 0), \quad (\widehat{q}_v)_k(\mathbf{x}, 0) = 0 \quad \text{for } 2 \leq k \leq M, \\ (\widehat{q}_c)_k(\mathbf{x}, 0) &= (\widehat{q}_r)_k(\mathbf{x}, 0) = 0 \quad \text{for } 0 \leq k \leq M. \end{aligned}$$

We compute the solution using different meshes until the final time $t = 100s$.

The experimental convergence study for the cloud and flow variables is presented in Tables 3 and 4, respectively. Similarly to the deterministic case, one can observe second-order convergence in space and time. In order to test the convergence in the stochastic space, we obtain a reference solution computed by the stochastic collocation method (see, e.g., [8]) with 20 Gauss-Legendre points. In Tables 5 and 6, the L^2 -norms of the coefficients of both stochastic Galerkin ($\|(\widehat{\rho q \ell})_k\|_{L^2(\Omega)}$) and stochastic collocation ($\|(\widetilde{\rho q \ell})_k\|_{L^2(\Omega)}$) methods for $\ell \in \{v, c, r\}$ and $k = 0, \dots, 3$ are shown at times $t = 50$ and $t = 100$, respectively. One can observe good agreement between both methods that demonstrates a good approximability property of the stochastic Galerkin method. Figure 9 shows the convergence of the stochastic approximation by comparing two subsequent solutions obtained by the stochastic Galerkin method using a mesh with 160×160 cells and $\Delta t = 0.01$ at time $t = 20s$. We can clearly see the spectral convergence with the rate $e^{-0.5M}$. Similarly, the spectral convergence obtained by the stochastic Galerkin method is demonstrated in Figure 10, where the errors between the approximated solution and the reference solution computed with 16 stochastic modes is plotted. The convergence rate is now $e^{-0.3M}$. Figure 11 illustrates the decreasing behavior of the L^2 -norm for the stochastic coefficients $\|(\widetilde{\rho q \ell})_k\|_{L^2(\Omega)}$ and $\|(\widehat{\rho q \ell})_k\|_{L^2(\Omega)}$ with respect to the stochastic modes m for both the stochastic collocation and stochastic Galerkin method. Our numerical simulations indicate that the stochastic Galerkin approximation is more accurate than the collocation method, in particular for the rain concentration. Analogously as in Figure 9 and Figure 10 the exponential decay with respect to m has been obtained.

N	L^1 -error in ρq_v	EOC	L^1 -error in ρq_c	EOC	L^1 -error in ρq_r	EOC
10	3.604e+03	–	2.029e+01	–	1.143e+03	–
20	9.062e+02	1.99	5.375e+00	1.92	1.618e-07	32.72
40	2.624e+02	1.79	1.698e+00	1.66	4.940e-08	1.71
80	7.364e+01	1.83	5.033e-01	1.75	1.379e-08	1.84
160	1.989e+01	1.89	1.396e-01	1.85	3.477e-09	1.99

TABLE 3. *Example 4: L^1 -errors and the corresponding EOCs for the cloud variables computed at the final time $t = 100s$ using $\Delta t = 20/N$ and $M = 3$.*

7.2. Rayleigh-Bénard convection. In this section, we present results of uncertainty study for the Rayleigh-Bénard convection in both 2-D and 3-D. We investigate uncertainty propagation, which is triggered either by the initial data or cloud parameters.

N	L^1 -error in ρ'	EOC	L^1 -error in ρu_1	EOC	L^1 -error in ρu_2	EOC	L^1 -error in $(\rho\theta)'$	EOC
10	1.113e+04	–	1.384e+06	–	1.745e+06	–	3.055e+06	–
20	1.207e+03	3.20	3.461e+05	2.00	3.007e+05	2.54	3.157e+05	3.27
40	2.903e+02	2.06	1.195e+05	1.53	9.919e+04	1.60	7.371e+04	2.10
80	9.289e+01	1.64	3.116e+04	1.94	2.892e+04	1.78	2.566e+04	1.52
160	2.527e+01	1.88	8.995e+03	1.79	8.417e+03	1.78	7.174e+03	1.84

TABLE 4. Example 4: L^1 -errors and the corresponding EOCs for the flow variables computed at the final time $t = 100s$ using $\Delta t = 20/N$ and $M = 3$.

m	$\ \widehat{\rho q}_v\ _{L^2}$	$\ \widetilde{\rho q}_v\ _{L^2}$	$\ \widehat{\rho q}_v - \widetilde{\rho q}_v\ _{L^2}$	$\ \widehat{\rho q}_c\ _{L^2}$	$\ \widetilde{\rho q}_c\ _{L^2}$	$\ \widehat{\rho q}_c - \widetilde{\rho q}_c\ _{L^2}$	$\ \widehat{\rho q}_r\ _{L^2}$	$\ \widetilde{\rho q}_r\ _{L^2}$	$\ \widehat{\rho q}_r - \widetilde{\rho q}_r\ _{L^2}$
0	5.74e+01	5.74e+01	3.60e-04	1.07e-01	1.07e-01	2.78e-06	4.03e-10	4.03e-10	2.24e-14
1	5.73e+00	5.73e+00	8.62e-03	2.14e-02	2.13e-02	5.75e-05	1.54e-10	1.53e-10	3.35e-13
2	5.01e-04	1.08e-03	7.74e-04	5.01e-04	4.97e-04	6.67e-06	1.31e-11	1.30e-11	8.25e-14
3	2.51e-05	2.77e-05	1.42e-05	2.67e-05	2.44e-05	4.64e-06	3.26e-13	3.29e-13	5.74e-15

TABLE 5. Example 4: Comparison of the L^2 -norms of stochastic coefficients $(\widehat{\rho q}_\ell)_k$ and $(\widetilde{\rho q}_\ell)_k$, $\ell \in \{v, c, r\}$ and $k = 0, \dots, 3$, obtained by both the stochastic Galerkin and stochastic collocation methods. Solutions are computed at time $t = 50s$ using $\Delta t = 0.01$ and $N = 160$.

m	$\ \widehat{\rho q}_v\ _{L^2}$	$\ \widetilde{\rho q}_v\ _{L^2}$	$\ \widehat{\rho q}_v - \widetilde{\rho q}_v\ _{L^2}$	$\ \widehat{\rho q}_c\ _{L^2}$	$\ \widetilde{\rho q}_c\ _{L^2}$	$\ \widehat{\rho q}_c - \widetilde{\rho q}_c\ _{L^2}$	$\ \widehat{\rho q}_r\ _{L^2}$	$\ \widetilde{\rho q}_r\ _{L^2}$	$\ \widehat{\rho q}_r - \widetilde{\rho q}_r\ _{L^2}$
0	5.70e+01	5.70e+01	3.09e-03	3.00e-01	3.00e-01	4.86e-05	6.64e-09	6.64e-09	3.45e-12
1	5.67e+00	5.66e+00	7.54e-02	5.99e-02	5.95e-02	8.53e-04	2.57e-09	2.56e-09	2.94e-11
2	1.39e-03	7.13e-03	6.67e-03	1.40e-03	1.36e-03	1.04e-04	2.28e-10	2.24e-10	7.30e-12
3	5.20e-05	9.84e-05	9.10e-05	5.62e-05	5.22e-05	7.77e-06	6.40e-12	6.24e-12	5.69e-13

TABLE 6. Example 4: Same as Table ?? but for the solutions computed at time $t = 100s$.

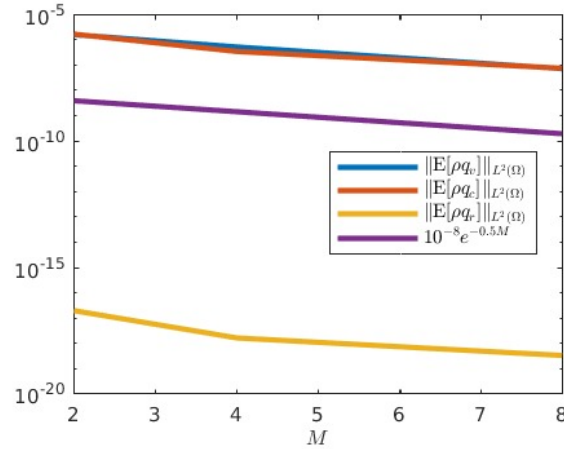


FIGURE 9. Example 4: Convergence study of the expected values of $(\rho q_\ell)_k$, $\ell \in \{v, c, r\}$, in the stochastic space at $t = 20s$ on a 160×160 mesh using $\Delta t = 0.01$.

Example 5: 2-D case with stochastic initial data. We begin by considering the following stochastically perturbed initial data for the cloud variables:

$$\begin{aligned}
(\widehat{q}_v)_0(\mathbf{x}, 0) &= 2 \cdot 10^{-5} \bar{\theta}, (\widehat{q}_v)_1(\mathbf{x}, 0) = 0.1(\widehat{q}_v)_0(\mathbf{x}, 0), (\widehat{q}_v)_k = 0 \quad \text{for } 2 \leq k \leq M, \\
(\widehat{q}_c)_k(\mathbf{x}, 0) &= (\widehat{q}_r)_k(\mathbf{x}, 0) = 0 \quad \text{for } 0 \leq k \leq M.
\end{aligned} \tag{7.1}$$

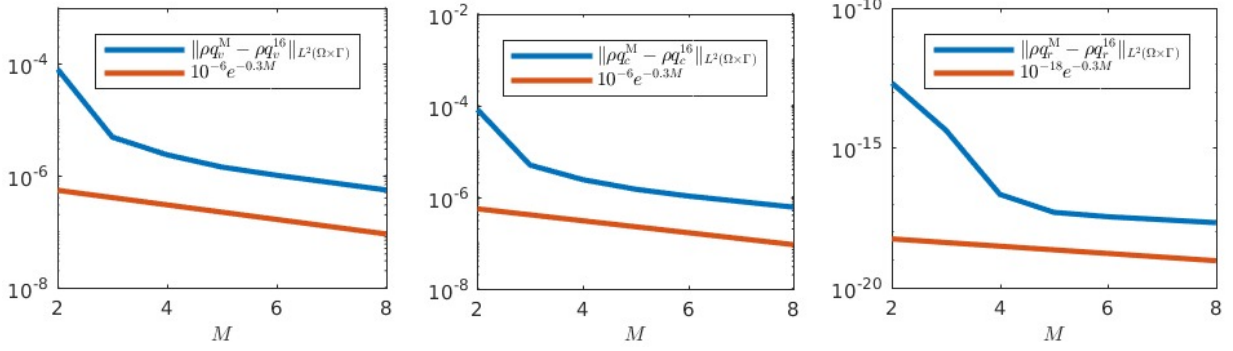


FIGURE 10. *Example 4: Convergence study of the functions (ρq_i) , $i = v, c, r$, in the stochastic space at $t = 20s$ on a 160×160 mesh using $\Delta t = 0.01$.*

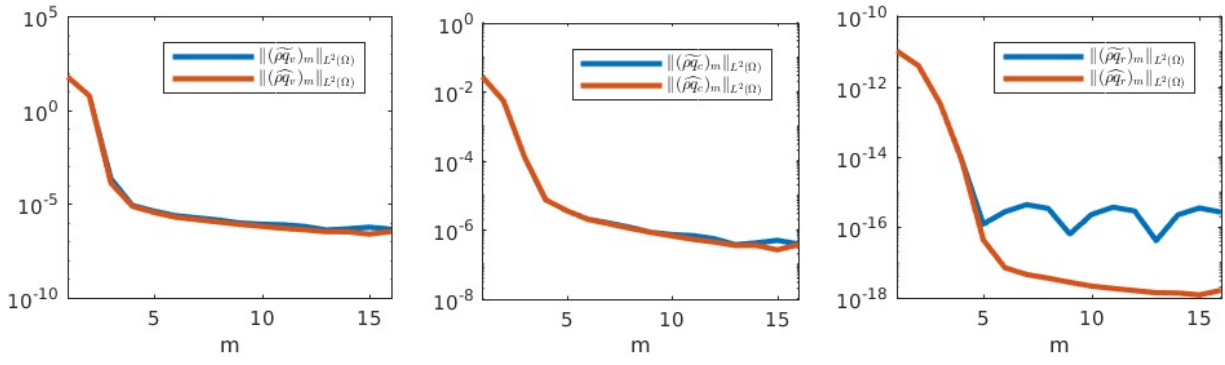


FIGURE 11. *Example 4: Behavior of the $L^2(\Omega)$ -norms of stochastic coefficients $(\widehat{\rho q}_\ell)_k$ and $(\widetilde{\rho q}_\ell)_k$, $\ell \in \{v, c, r\}$ computed by the stochastic Galerkin and stochastic collocation methods, respectively, at time $t = 20s$ on a 160×160 mesh using $\Delta t = 0.01$.*

The numerical solution computed using 320×320 mesh cells is presented at two times $t = 1600s$ and $t = 2200s$ in Figures 12–15, for the potential temperature θ , water vapor q_v , cloud drops q_c and rain q_r , respectively. Figures 13–15 show both the expected value $\mathbb{E}[\rho q_i]$ and the standard deviation $\sigma(\rho q_\ell)$ of the cloud variables, $\ell \in \{v, c, r\}$. The evolution of uncertainties in structures can be clearly observed, in particular, in the evolution of the standard deviation. It is well-known that the structure formation is quite sensitive to the size of perturbation. In order to illustrate this phenomenon, we have also perturbed the initial water vapor concentration by 5% and 20%, that is, by setting

$$(\widehat{q}_v)_1(\mathbf{x}, 0) = 0.05(\widehat{q}_v)_0(\mathbf{x}, 0) \quad \text{and} \quad (\widehat{q}_v)_1(\mathbf{x}, 0) = 0.2(\widehat{q}_v)_0(\mathbf{x}, 0),$$

respectively. Figures 16–18 show the numerical solution for the potential temperature θ and expected values of the cloud drops ($\mathbb{E}[\rho q_c]$) and rain ($\mathbb{E}[\rho q_r]$) computed using 320×320 mesh cells until the final time $t = 2200s$. We can clearly recognize different structures and larger smearing for 20% perturbation of the initial water vapor concentration.

Example 6: 2-D case with stochastic parameters. In the following experiment, we study uncertainty propagation due to incomplete information about the model parameters which is a very typical problem arising in atmospheric science. We chose the same initial data for the flow and cloud variables as in Section 6.2. More precisely, we take the following initial cloud variables:

$$(\widehat{q}_v)_0(\mathbf{x}, 0) = 0.02\theta'(\mathbf{x}, 0), \quad (\widehat{q}_v)_k(\mathbf{x}, 0) = (\widehat{q}_c)_k(\mathbf{x}, 0) = (\widehat{q}_r)_k(\mathbf{x}, 0) = 0 \quad \text{for } 1 \leq k \leq M.$$

As pointed out in [40], suitable parameters for the sensitivity study are k_1 , k_2 and α , see Section 2. Consequently, in order to investigate uncertainty propagation in the numerical solution we choose 10%, 20% and

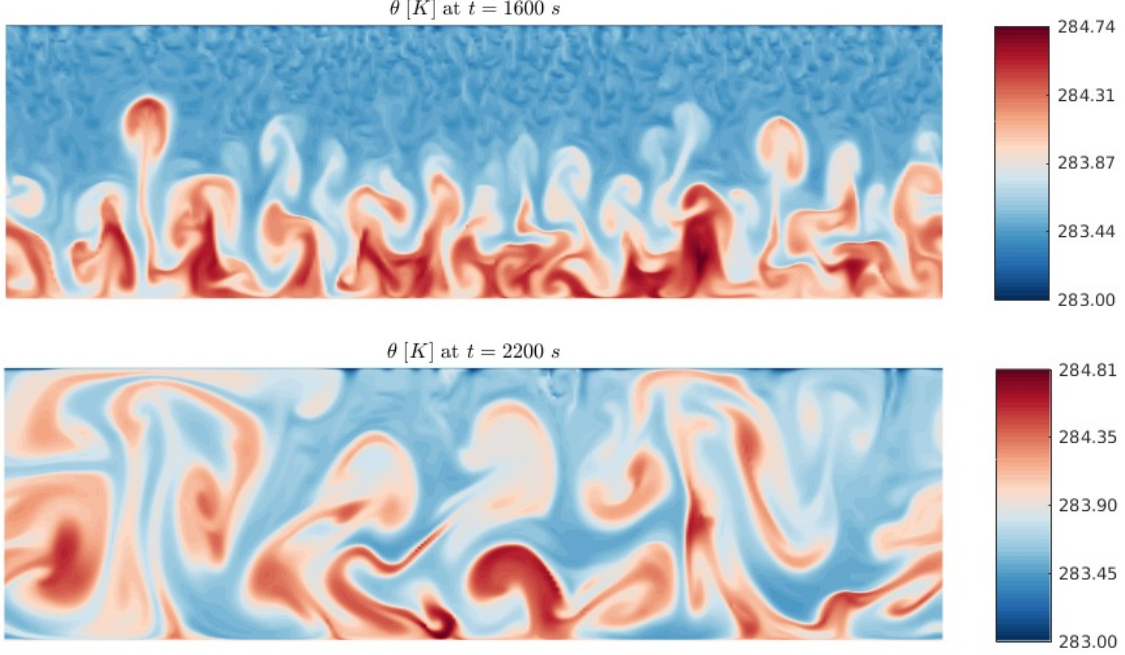


FIGURE 12. *Example 5: Potential temperature θ at times $t = 1600s$ and $2200s$ using 10% perturbation of the initial data in q_v .*

50% perturbation of these coefficients, that is, we take

$$\begin{aligned}
 (\hat{k}_1)_0 &= 0.0041, & (\hat{k}_1)_1 &= p(\hat{k}_1)_0, & (\hat{k}_1)_k &= 0 \quad \text{for } 2 \leq k \leq M, \\
 (\hat{k}_2)_0 &= 0.8, & (\hat{k}_2)_1 &= p(\hat{k}_2)_0, & (\hat{k}_2)_k &= 0 \quad \text{for } 2 \leq k \leq M, \\
 \hat{\alpha}_0 &= 190.3, & \hat{\alpha}_1 &= p\hat{\alpha}_0, & \hat{\alpha}_k &= 0 \quad \text{for } 2 \leq k \leq M,
 \end{aligned}$$

where $p = 0.1, 0.2$ and 0.5 , respectively. The numerical solution is computed using a mesh with 320×320 cells until the final time $t = 2200s$. Figures 19–22 present the potential temperature θ , the expected values of the water vapor concentration q_v , the cloud drops concentration q_c and the rain concentration q_r , respectively. The standard deviation for the cloud variables is shown in Figures 23–25. As one can see in Figures 20–22, the structures in expected values vary quite considerably, though quantitative changes are quite small for different parameter perturbations. One can also notice that the standard deviation for the cloud variables varies considerably both qualitatively and quantitatively. Thus, our numerical study indicates that the cloud model (2.2) is quite sensitive to the chosen set of model parameters.

Example 7: 3-D case with stochastic initial data. Similarly to Example 5, we now investigate the uncertainty quantification in the 3-D Raleigh-Bénard convection for stochastically perturbed initial data of the cloud variables given by (7.1). The numerical solution is computed in a domain $\Omega = [0, 5000] \times [0, 5000] \times [0, 1000] [m^3]$, which is discretized using $50 \times 50 \times 50$ mesh cells. In Figure 26, we show the time evolution for the potential temperature θ at times $t = 1600, 2200, 2800$ and $3600s$. As expected, hexagonal structures are formed. In order to visualize these structures, we once again plot the solution in a slightly smaller domain $[0, 5000] \times [0, 5000] \times [0, 970] [m^3]$. In Figures 27–29, we present the time evolution of the expected values of the concentrations of water vapor q_v , cloud drops q_c and rain q_r , respectively. As expected, the structures in the numerical solution with stochastically perturbed initial data are more smeared in comparison to the deterministic solution shown in Figures 5–8.

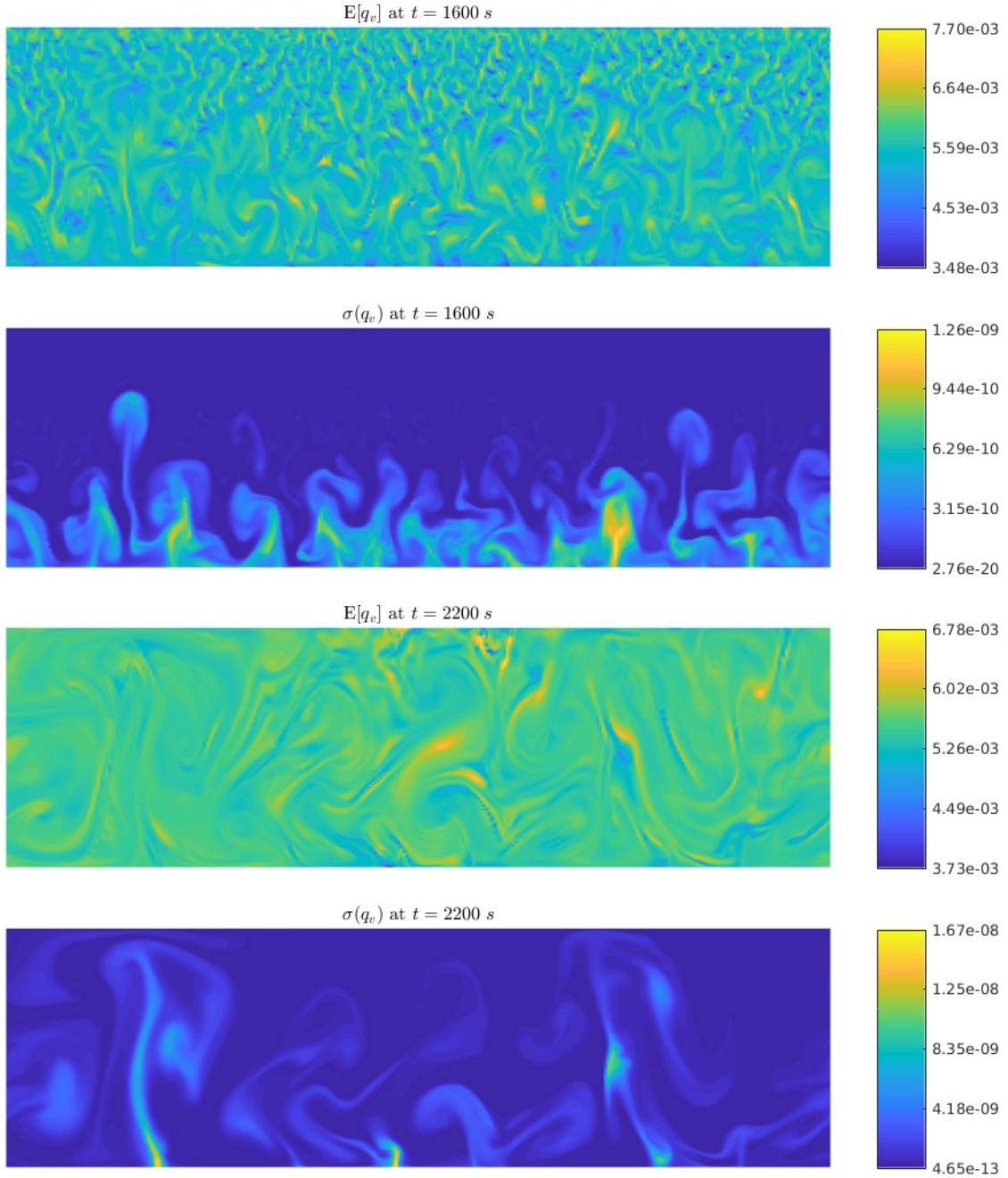


FIGURE 13. *Example 5: Expected value and standard deviation for the water vapor concentration q_v at times $t = 1600$ s and 2200 s using 10% perturbation of the initial data in q_v .*

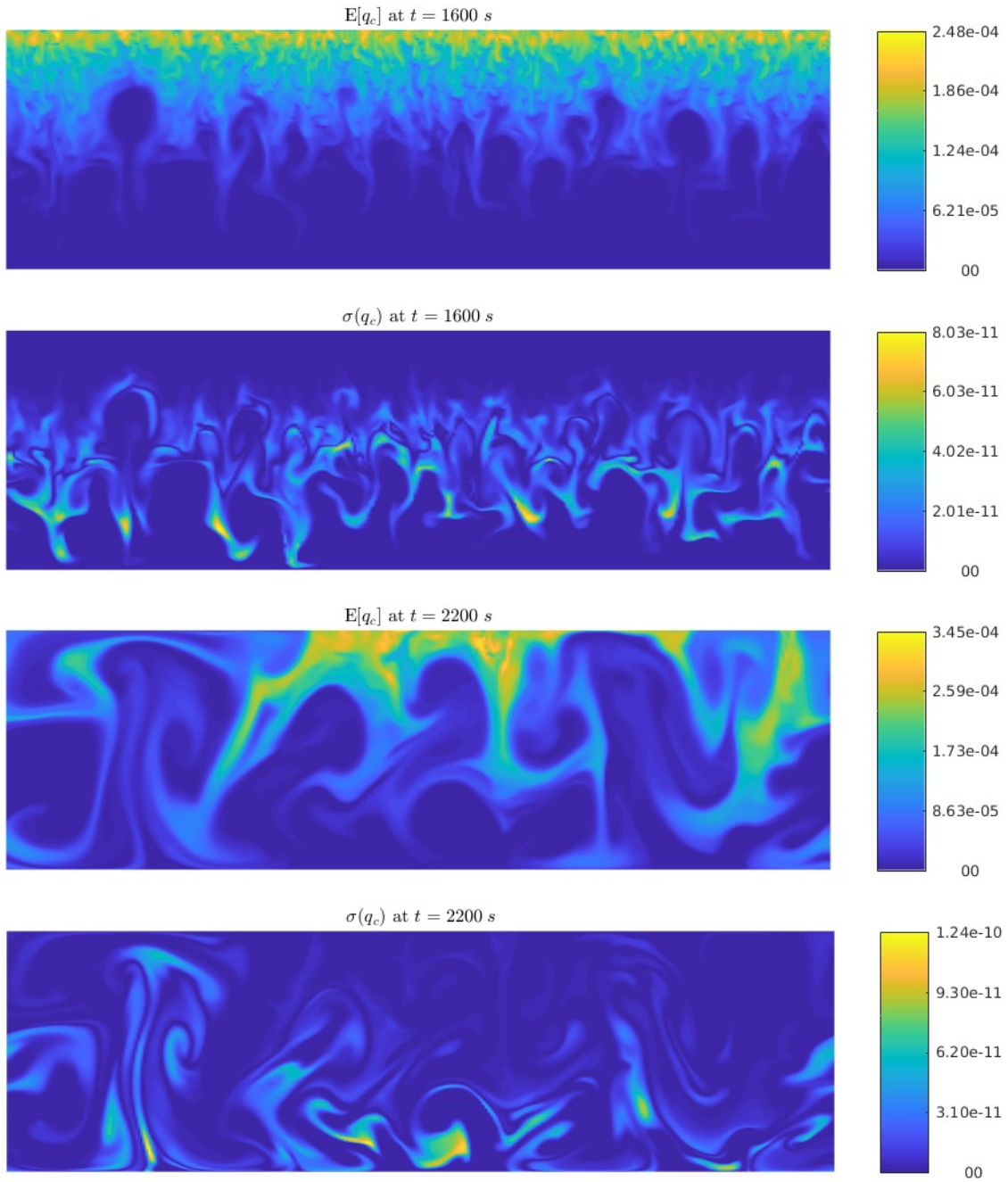


FIGURE 14. *Example 5: Expected value and standard deviation for the cloud drops concentration q_c at times $t = 1600$ s and 2200 s using 10% perturbation of the initial data in q_v .*

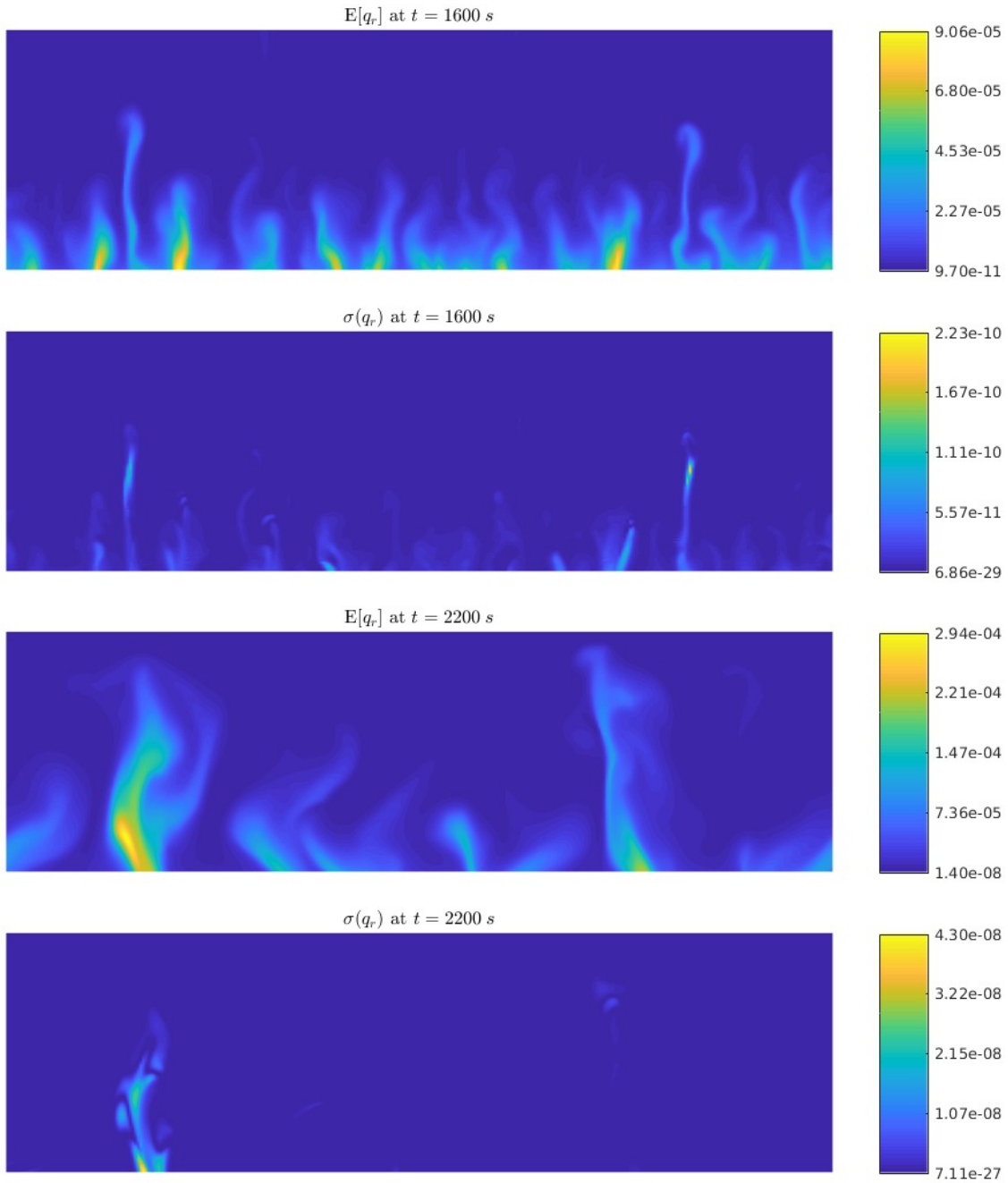


FIGURE 15. Example 5: Expected value and standard deviation for the rain concentration q_r at times $t = 1600$ s and 2200 s using 10% perturbation of the initial data in q_v .

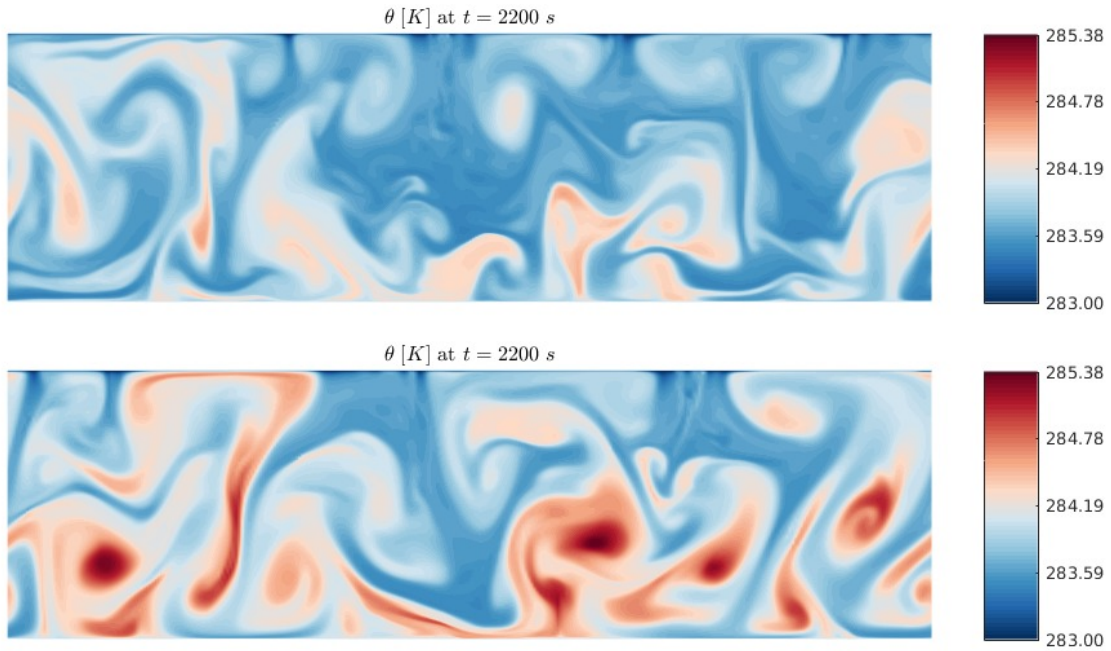


FIGURE 16. Example 5: Potential temperature θ computed at time $t = 2200$ s using 5% and 20% perturbation of the initial data in q_v .

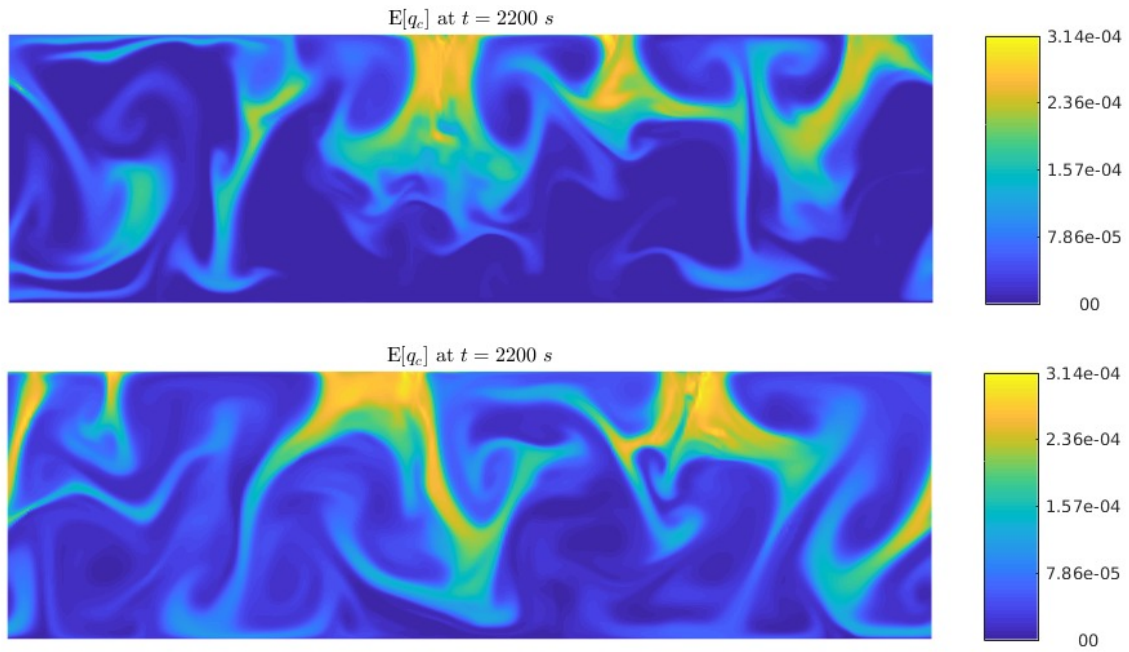


FIGURE 17. Example 5: Expected values for the cloud drops concentration q_c computed at time $t = 2200$ s using 5% and 20% perturbation of the initial data in q_v .

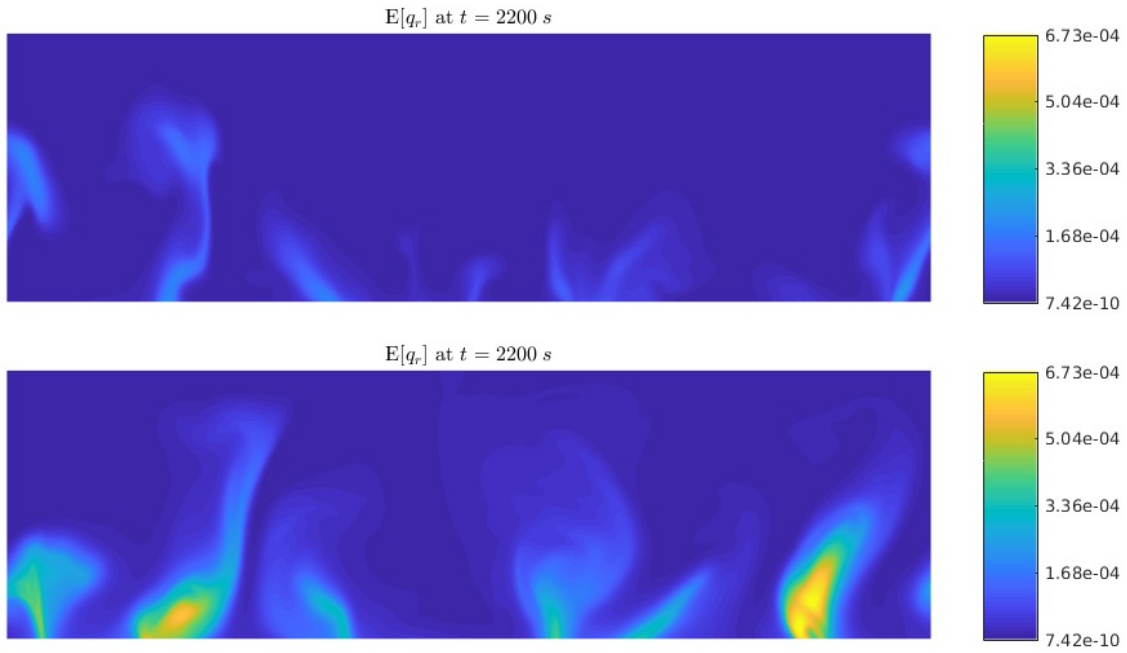


FIGURE 18. *Example 5: Expected values for the rain concentration q_r computed at time $t = 2200$ s using 5% and 20% perturbation of the initial data in q_v .*

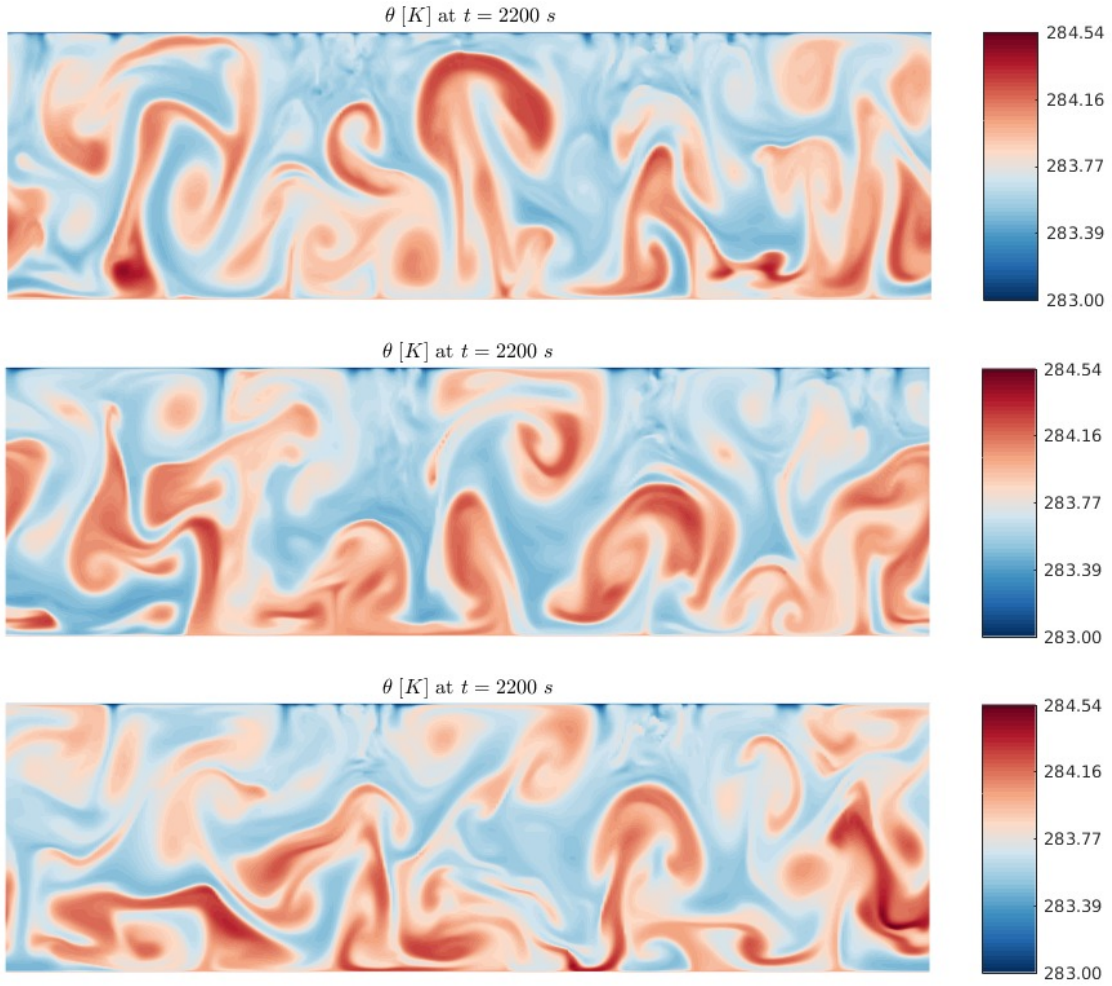


FIGURE 19. *Example 6: Potential temperature θ computed at time $t = 2200$ s using 10%, 20% and 50% perturbation of the cloud parameters.*

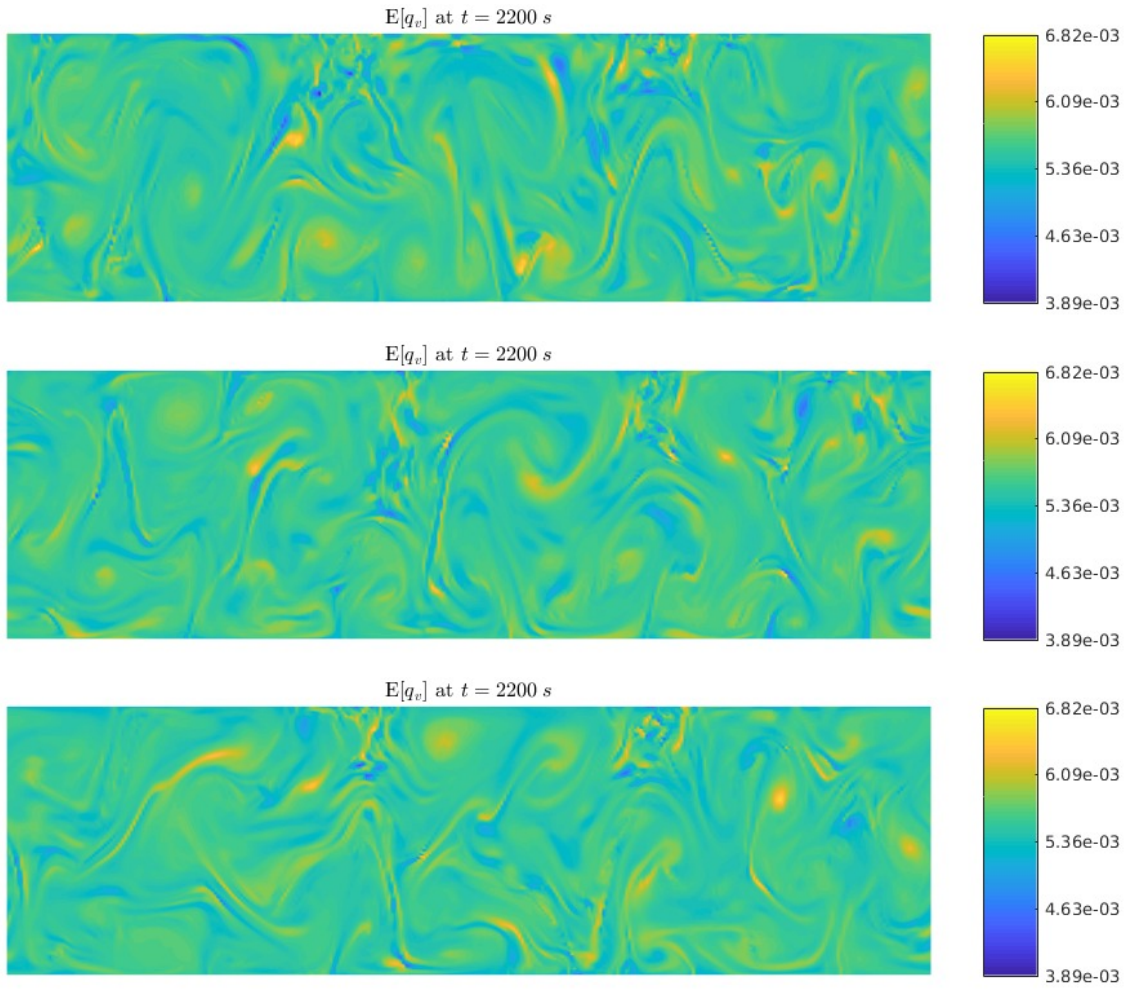


FIGURE 20. *Example 6: Expected value for the water vapor concentration q_v computed at time $t = 2200$ s using 10%, 20% and 50% perturbation of the cloud parameters.*

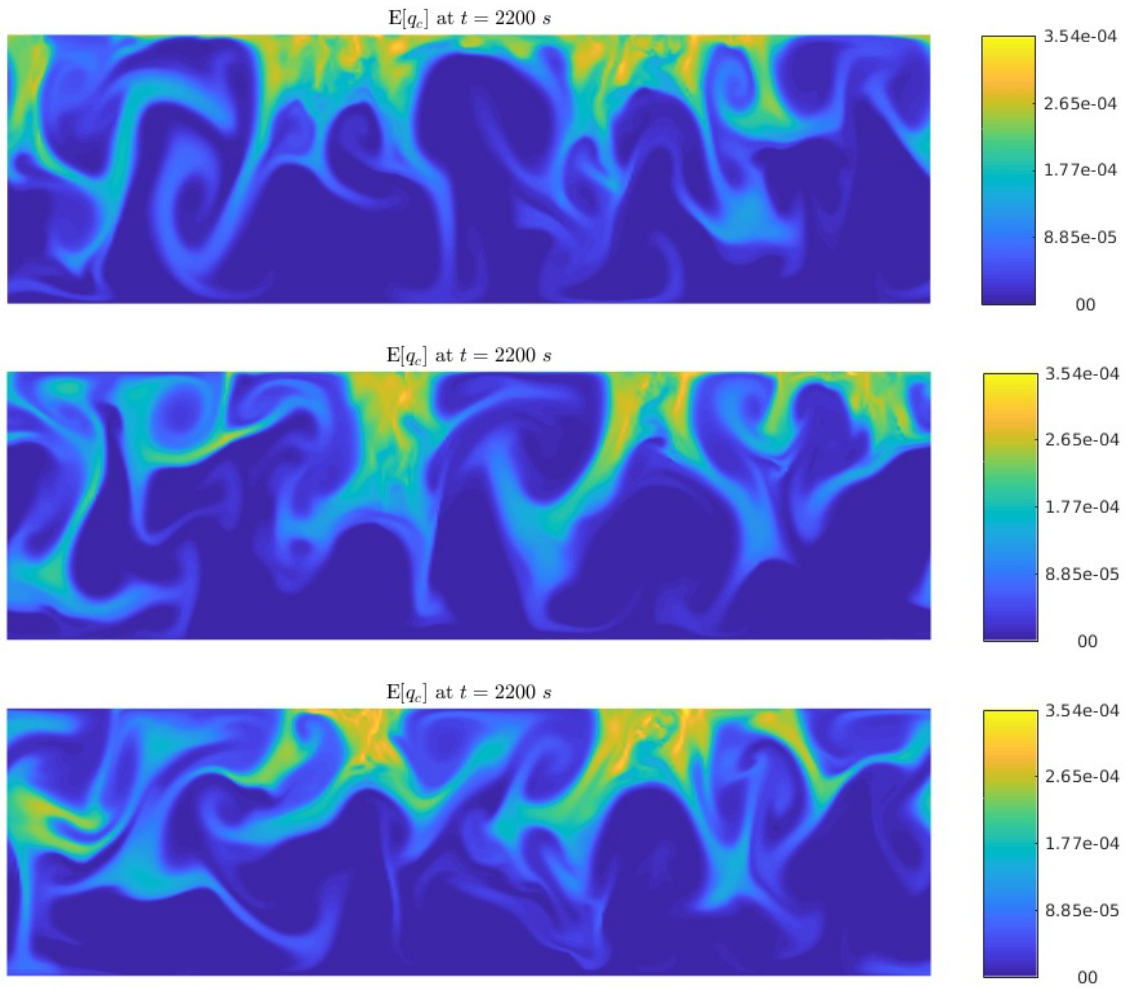


FIGURE 21. *Example 6: Expected value for the cloud drop concentration q_c computed at time $t = 2200$ s using 10%, 20% and 50% perturbation of the cloud parameters.*

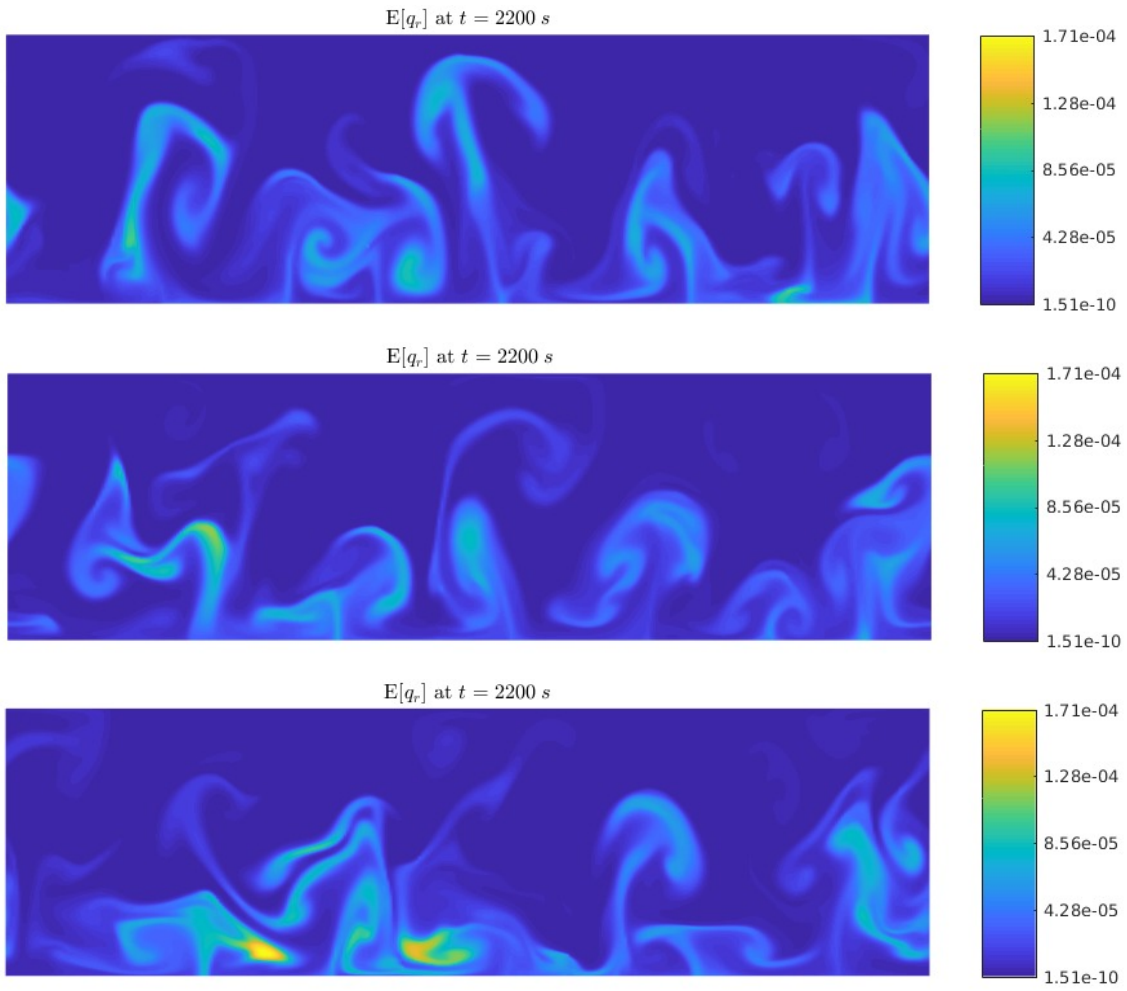


FIGURE 22. *Example 6: Expected value for the rain concentration q_r computed at time $t = 2200$ s using 10%, 20% and 50% perturbation of the cloud parameters.*

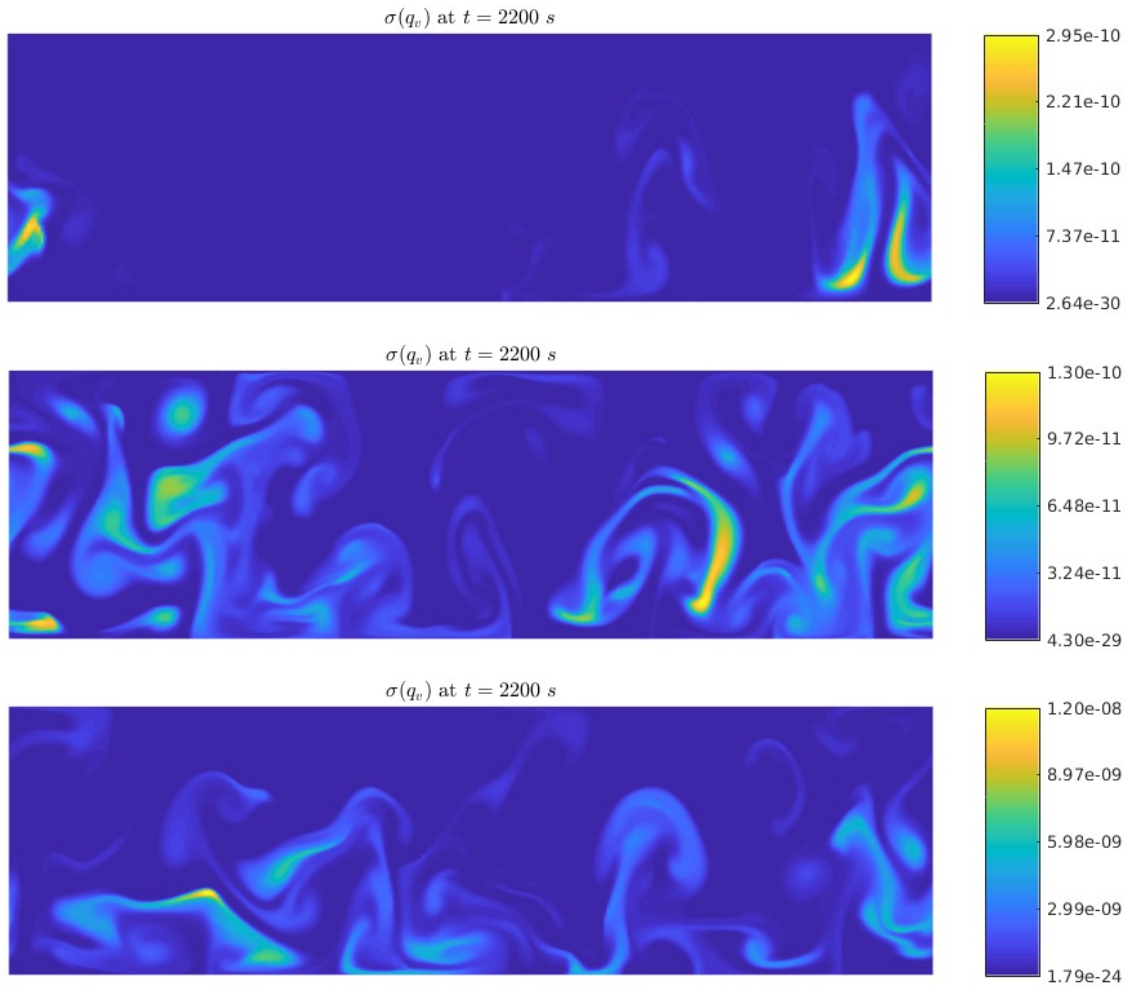


FIGURE 23. *Example 6: Standard deviation for the water vapor concentration q_v computed at time $t = 2200$ s using 10%, 20% and 50% perturbation of the cloud parameters.*

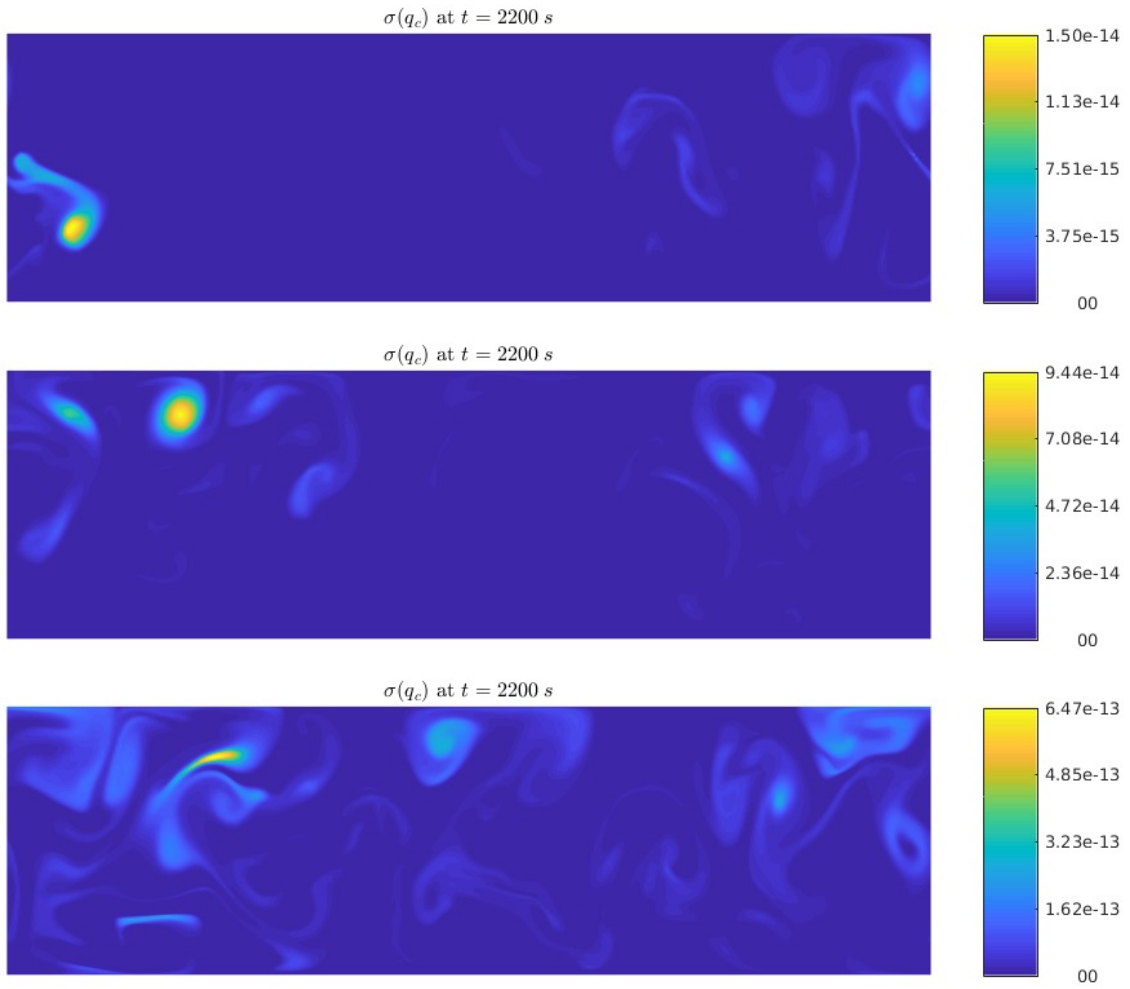


FIGURE 24. *Example 6: Standard deviation for the cloud drop concentration q_c computed at time $t = 2200$ s using 10%, 20% and 50% perturbation of the cloud parameters.*

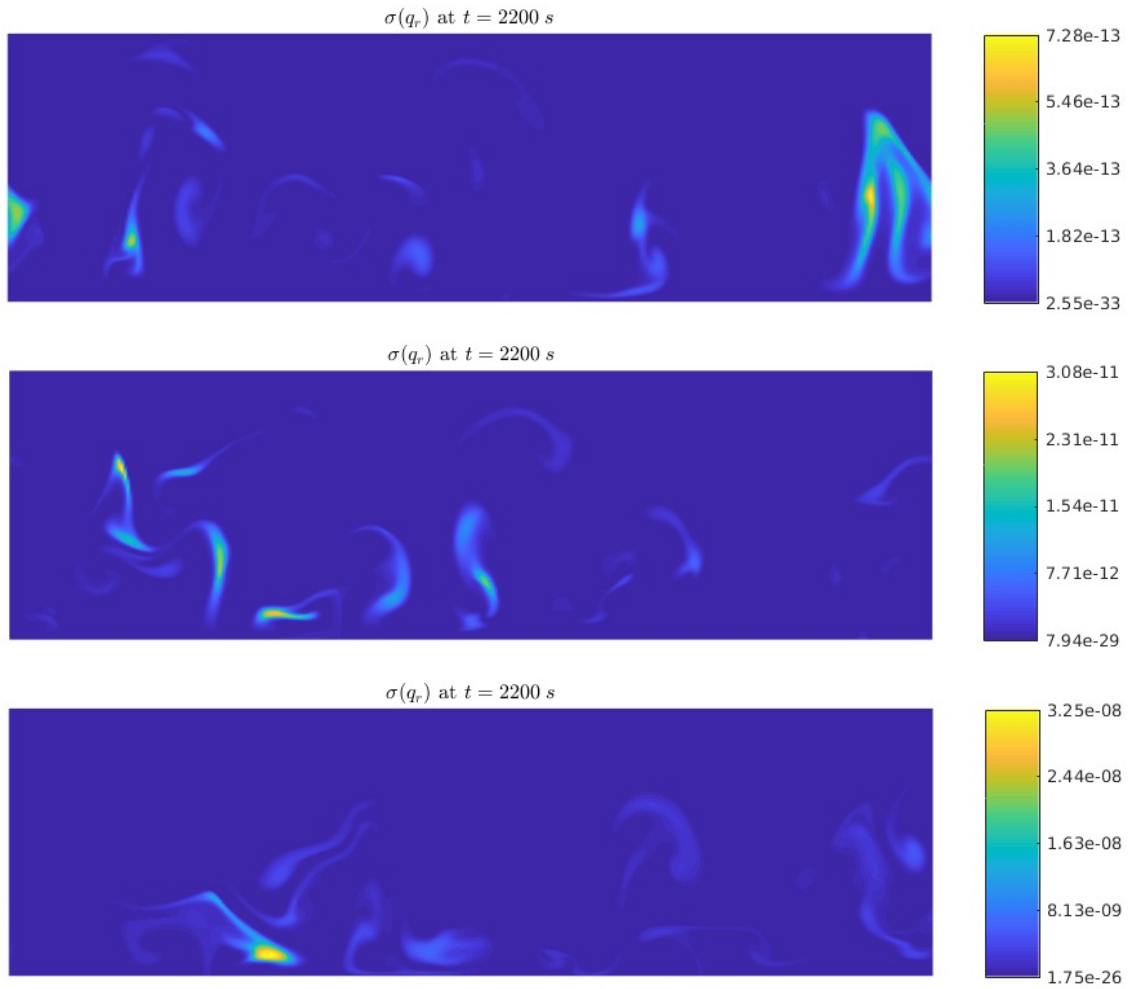


FIGURE 25. *Example 6: Standard deviation for the rain concentration q_r computed at time $t = 2200$ s using 10%, 20% and 50% perturbation of the cloud parameters.*

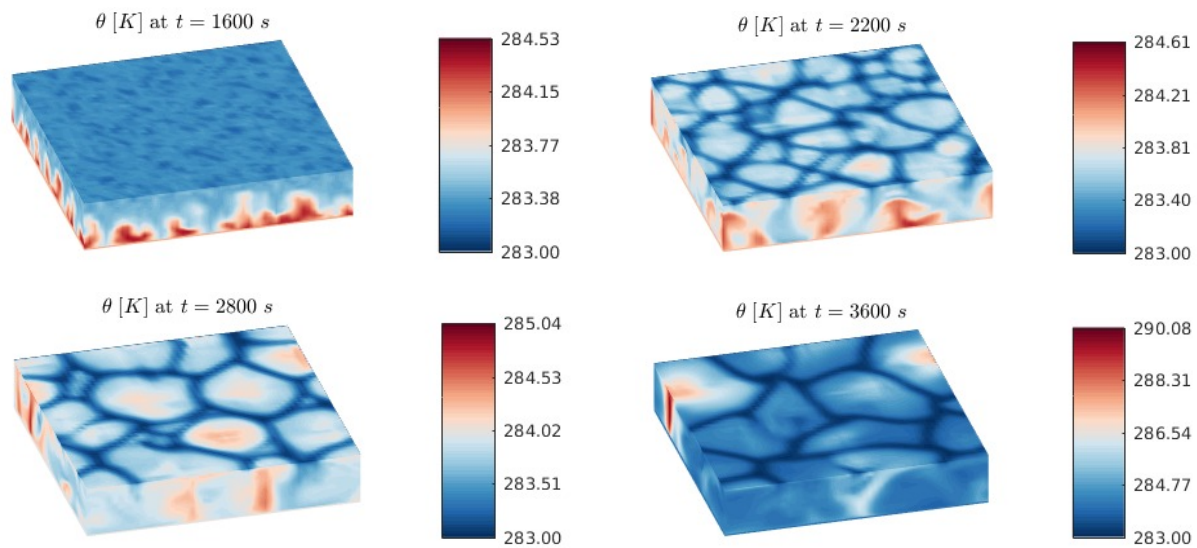


FIGURE 26. *Example 7: Time evolution of the potential temperature θ .*

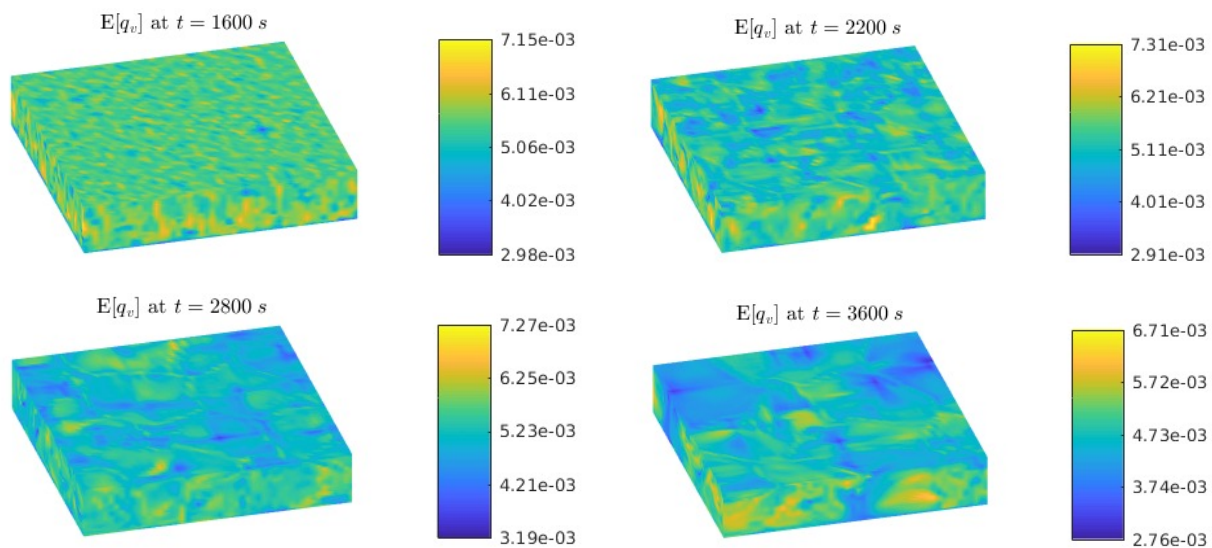


FIGURE 27. *Example 7: Time evolution of the expected value of the water vapor concentration q_v .*

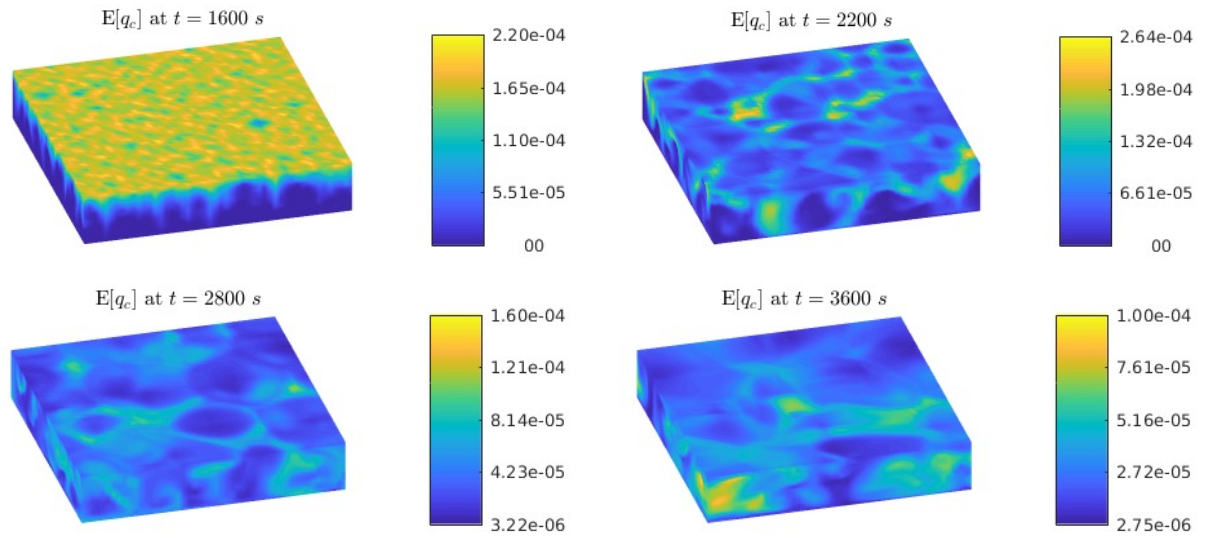


FIGURE 28. *Example 7: Time evolution of the expected value of the cloud drops concentration q_c .*

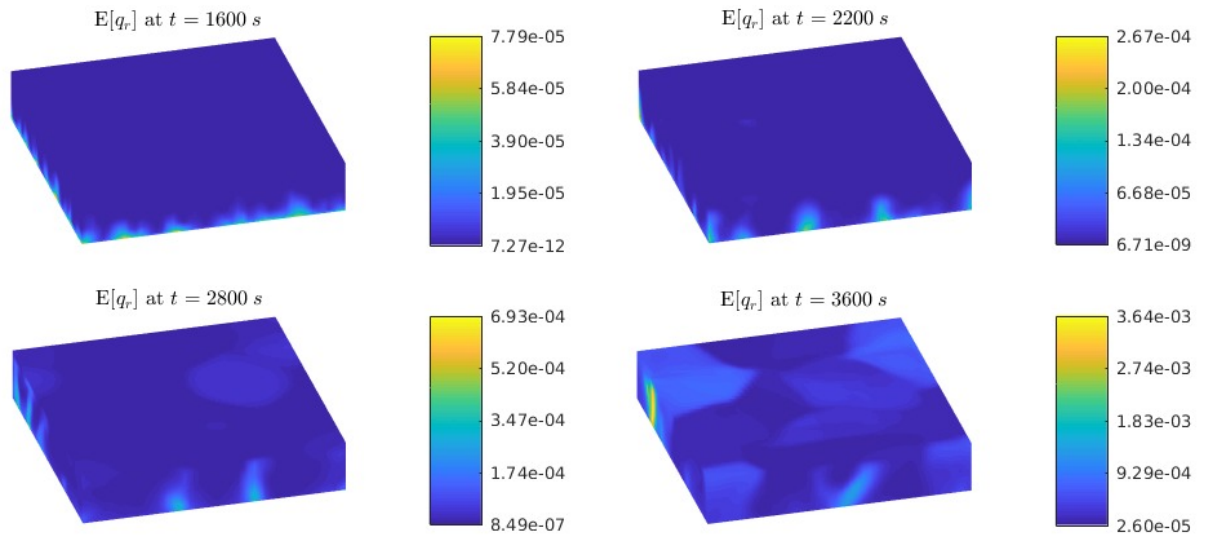


FIGURE 29. *Example 7: Time evolution of the expected value of the rain concentration q_r .*

8. CONCLUSION

In the present paper, we have studied uncertainty propagation in an atmospheric model that combines the Navier-Stokes equations for weakly compressible fluids (2.1) with the cloud equations (2.2). The latter has been recently proposed in [40] and is based on the so-called single moment approach considering the evolution equations for the mass concentrations of the water vapor, cloud drops and rain. Our numerical strategy is based on the stochastic Galerkin method that combines a finite-volume method for space-time discretization with a spectral approximation in the stochastic space. We point out that atmospheric flows are weakly compressible which leads to the low Mach number problem. One therefore needs to use a finite-volume method, which is accurate and efficient in the low Mach number regime; see [5, 6]. To this end, we have chosen a suitable linear-nonlinear splitting between the fast and slow flow variables and the second-order IMEX discretization in time (the ARS (2,2,2) scheme) as described in Section 4. Coupling between the cloud model (2.2) and the Navier-Stokes system (2.8) is realized numerically by the second-order Strang splitting. The cloud equations are approximated in space by the finite-volume method and in time using the explicit third-order Runge-Kutta method with an enlarged stability region as explained in Section 4. Note that microscopic cloud dynamics requires a smaller time step than the flow dynamics and thus several microscopic cloud subiterations are realized within one macroscopic splitting time step, whose size is dictated by the flow dynamics. To the best of our knowledge, this is the first contribution that combines an accurate and efficient method for the weakly compressible Navier-Stokes equations with the stochastic Galerkin method for the uncertainty quantification of time evolution of the mass densities of water vapor, cloud drops and rain.

We have conducted extensive numerical benchmarking for both the deterministic and stochastic models and present the obtained numerical results in Sections 6 and 7. In the latter, we took into account the uncertainties in both initial data and cloud model parameters. Our numerical study clearly demonstrates applicability of the stochastic Galerkin method for the uncertainty quantification in complex atmospheric models. Our future goal is to extend the developed numerical method to the fully random Navier-Stokes-cloud system by considering random weakly compressible Navier-Stokes equations. This will allow one to quantify more precisely the propagation of small scale stochastic errors initiated at cloud scales to macroscopic scales of flow dynamics.

Acknowledgement

The research leading to these results has been done within the sub-project A2 of the Transregional Collaborative Research Center SFB/TRR 165 “Waves to Weather” funded by the German Science Foundation (DFG). The work of A. Chertock was supported in part by NSF grants DMS-1521051 and DMS-1818684. The work of A. Kurganov was supported in part by NSFC grant 11771201 and NSF grants DMS-1521009 and DMS-1818666.

The authors gratefully acknowledge the support of the Data Center ZDV in Mainz for providing computation time on MOGON and MOGON II clusters and of NSF RNMS Grant DMS-1107444 (KI-Net).

REFERENCES

- [1] T. Alboussière and Y. Ricard. Rayleigh-Bénard stability and the validity of quasi-Boussinesq or quasi-anelastic liquid approximations. *J. Fluid Mech.*, 817:264–305, 2017.
- [2] U. M. Ascher, S. J. Ruuth, and R. J. Spiteri. Implicit-explicit Runge-Kutta methods for time-dependent partial differential equations. *Appl. Numer. Math.*, 25(2-3):151–167, 1997. Special issue on time integration (Amsterdam, 1996).
- [3] M. Baldauf, J. Förstner, S. Klink, T. Reinhardt, C. Schraff, A. Seifert, and K. Stephan. Kurze modell- und datenbankbeschreibung COSMO-DE (LMK). 2014.
- [4] K. D. Beheng. The Evolution of Raindrop Spectra: A Review of Microphysical Essentials. In F. Y. Testik and M. Gebre-michael, editors, *Rainfall: State of the Science*, Geophysical Monograph Series, pages 29–48, 2010.
- [5] G. Bispen. IMEX finite volume schemes for the shallow water equations, PhD thesis. Johannes Gutenberg-University, Mainz, 2015.
- [6] G. Bispen, M. Lukáčová-Medvid'ová, and L. Yelash. Asymptotic preserving IMEX finite volume schemes for low Mach number Euler equations with gravitation. *J. Comput. Phys.*, 2017.
- [7] G. H. Bryan and J. M. Fritsch. A benchmark simulation for moist nonhydrostatic numerical models. *Mont. Weather Rev.*, 130:2917–2928, 2002.

- [8] C. Canuto. *Spectral Methods - Fundamentals in Single Domains*. Springer, 2006.
- [9] Q.-Y. Chen, D. Gottlieb, and J. S. Hesthaven. Uncertainty analysis for the steady-state flows in a dual throat nozzle. *J. Comput. Phys.*, 204(1):378–398, 2005.
- [10] R. M. Davies and F. J. Taylor. The mechanism of large bubbles rising through extended liquids and through liquids in tubes. *Proc. Royal Soc. Lond. A*, 200:375–390, 1950.
- [11] B. Després, G. Poëtte, and D. Lucor. Robust uncertainty propagation in systems of conservation laws with the entropy closure method. In *Uncertainty Quantification in Computational Fluid Dynamics*, pages 105–149. Springer, 2013.
- [12] H. C. Elman, C. W. Miller, E. T. Phipps, and R. S. Tuminaro. Assessment of collocation and Galerkin approaches to linear diffusion equations with random data. *Int. J. Uncertain. Quantif.*, 1(1):19–33, 2011.
- [13] A. V. Getling. *Rayleigh-Bénard convection, Structure and Dynamics*. World Sci. Publ., Singapore, 2001.
- [14] D. Gottlieb and D. Xiu. Galerkin method for wave equations with uncertain coefficients. *Commun. Comput. Phys.*, 3(2):505–518, 2008.
- [15] W. W. Grabowski. Untangling microphysical impacts on deep convection applying a novel modeling methodology. *J. Atmos. Sci.*, 72(6):2446–2464, 2015.
- [16] J. Hu, S. Jin, and D. Xiu. A stochastic Galerkin method for Hamilton-Jacobi equations with uncertainty. *SIAM J. Sci. Comput.*, 37(5):A2246–A2269, 2015.
- [17] A. L. Igel and S. C. van den Heever. The role of latent heating in warm frontogenesis. *Quart. J. Roy. Met. Soc.*, 140(678, A):139–150, 2014.
- [18] S. Jin, D. Xiu, and X. Zhu. Asymptotic-preserving methods for hyperbolic and transport equations with random inputs and diffusive scalings. *J. Comput. Phys.*, 289:35–52, 2015.
- [19] E. Kessler. *On the distribution and continuity of water substance in atmospheric circulations.*, volume 32 of *Meteorol. Monographs*. American Meteorological Society, Boston, 1969.
- [20] A. P. Khain, K. D. Beheng, A. Heymsfield, A. Korolev, S. O. Krichak, Z. Levin, M. Pinsky, V. Phillips, T. Prabhakaran, A. Teller, S. C. van den Heever, and J.-I. Yano. Representation of microphysical processes in cloud-resolving models: Spectral (bin) microphysics versus bulk parameterization. *Rev. Geophys.*, 53(2):247–322, 2015.
- [21] A. P. Khain, M. Ovchinnikov, M. Pinsky, A. Pokrovsky, and H. Krugliak. Notes on the state-of-the-art numerical modeling of cloud microphysics. *Atmos. Res.*, 55(3-4):159 – 224, 2000.
- [22] V. I. Khvorostyanov. Mesoscale processes of cloud formation, cloud-radiation interaction, and their modeling with explicit cloud microphysics. *Atmos. Res.*, 39(1-3):1–67, 1995.
- [23] H. Köhler. The nucleus in and the growth of hygroscopic droplets. *T. Faraday Soc.*, 32(2):1152–1161, 1936.
- [24] A. Kurganov and G. Petrova. Central-upwind schemes for two-layer shallow water equations. *SIAM J. Sci. Comput.*, 31(3):1742–1773, 2009.
- [25] D. Lamb and J. Verlinde. *Physics and chemistry of clouds*. Cambridge University Press, 2011.
- [26] G. Lin, C. H. Su, and G. E. Karniadakis. The stochastic piston problem. *Proc. Natl. Acad. Sci. USA*, 101(45):15840–15845, 2004.
- [27] M. Lukáčová-Medvid’ová, J. Rosemeier, P. Spichtinger, and B. Wiebe. IMEX finite volume methods for cloud simulation. In *Finite volumes for complex applications VIII—hyperbolic, elliptic and parabolic problems*, volume 200 of *Springer Proc. Math. Stat.*, pages 179–187. Springer, Cham, 2017.
- [28] X. Ma and N. Zabarar. An adaptive hierarchical sparse grid collocation algorithm for the solution of stochastic differential equations. *J. Comput. Phys.*, 228(8):3084–3113, 2009.
- [29] P. J. Marinescu, S. C. van den Heever, S. M. Saleeby, S. M. Kreidenweis, and P. J. DeMott. The microphysical roles of lower-tropospheric versus midtropospheric aerosol particles in mature-stage mcs precipitation. *J. Atmos. Sci.*, 74(11):3657–3678, 2017.
- [30] J. S. Marshall and W. McK. Palmer. The distributions of raindrops with size. *J. Meteorol.*, 5:165–166, 1948.
- [31] A. A. Medovikov. Dumka 3 code, available at <http://dumkaland.org/>.
- [32] A. A. Medovikov. High order explicit methods for parabolic equations. *BIT*, 38(2):372–390, 1998.
- [33] S. Mishra and C. Schwab. Sparse tensor multi-level Monte Carlo finite volume methods for hyperbolic conservation laws with random initial data. *Math. Comp.*, 81(280):1979–2018, 2012.
- [34] S. Mishra, C. Schwab, and J. Šukys. Multi-level Monte Carlo finite volume methods for nonlinear systems of conservation laws in multi-dimensions. *J. Comput. Phys.*, 231(8):3365–3388, 2012.
- [35] S. Mishra, C. Schwab, and J. Šukys. Multilevel Monte Carlo finite volume methods for shallow water equations with uncertain topography in multi-dimensions. *SIAM J. Sci. Comput.*, 34(6):B761–B784, 2012.
- [36] S. Mishra, C. Schwab, and J. Šukys. Multi-level Monte Carlo finite volume methods for uncertainty quantification in nonlinear systems of balance laws. In *Uncertainty quantification in computational fluid dynamics*, volume 92 of *Lect. Notes Comput. Sci. Eng.*, pages 225–294. Springer, Heidelberg, 2013.
- [37] O. Pauluis and J. Schumacher. Idealized moist Rayleigh-Bénard convection with piecewise linear equation of state. *Comm. Math. Sci.*, 8:295–319, 2010.
- [38] M. D. Petters and S. M. Kreidenweis. A single parameter representation of hygroscopic growth and cloud condensation nucleus activity. *Atmos. Chem. Phys.*, 7(8):1961–1971, 2007.
- [39] G. Poëtte, B. Després, and D. Lucor. Uncertainty quantification for systems of conservation laws. *J. Comput. Phys.*, 228(7):2443–2467, 2009.
- [40] N. Porz, M. Hanke, M. Baumgartner, and P. Spichtinger. A consistent model for liquid clouds. *Math. Clim. Weather Forecast. (submitted)*, 2018.

- [41] R. Pulch and D. Xiu. Generalised polynomial chaos for a class of linear conservation laws. *J. Sci. Comput.*, 51(2):293–312, 2012.
- [42] D. Schuster, S. Brdar, M. Baldauf, A. Dedner, R. Klöfkorn, and D. Kröner. On discontinuous Galerkin approach for atmospheric flow in the mesoscale with and without moisture. *Meteorol. Z.*, 23(4):449–464, 2011.
- [43] J. Šukys, S. Mishra, and C. Schwab. Multi-level Monte Carlo finite difference and finite volume methods for stochastic linear hyperbolic systems. In *Monte Carlo and quasi-Monte Carlo methods 2012*, volume 65 of *Springer Proc. Math. Stat.*, pages 649–666. Springer, Heidelberg, 2013.
- [44] T. Tang and T. Zhou. Convergence analysis for stochastic collocation methods to scalar hyperbolic equations with a random wave speed. *Commun. Comput. Phys.*, 8(1):226–248, 2010.
- [45] J. Tryoen, O. Le Maître, and A. Ern. Adaptive anisotropic spectral stochastic methods for uncertain scalar conservation laws. *SIAM J. Sci. Comput.*, 34(5):A2459–A2481, 2012.
- [46] J. Tryoen, O. Le Maître, M. Ndjinga, and A. Ern. Intrusive Galerkin methods with upwinding for uncertain nonlinear hyperbolic systems. *J. Comput. Phys.*, 229(18):6485–6511, 2010.
- [47] J. Tryoen, O. Le Maître, M. Ndjinga, and A. Ern. Roe solver with entropy corrector for uncertain hyperbolic systems. *J. Comput. Appl. Math.*, 235(2):491–506, 2010.
- [48] X. Wan and G. E. Karniadakis. Long-term behavior of polynomial chaos in stochastic flow simulations. *Comput. Methods Appl. Mech. Engrg.*, 195(41-43):5582–5596, 2006.
- [49] J. Warner. The microstructure of cumulus cloud. part i. general features of the droplet spectrum. *J. Atmos. Sci.*, 26(5):1049–1059, 1969.
- [50] J. A. S. Witteveen, A. Loeven, and H. Bijl. An adaptive stochastic finite elements approach based on Newton-Cotes quadrature in simplex elements. *Comput. & Fluids*, 38(6):1270–1288, 2009.
- [51] D. Xiu and J. S. Hesthaven. High-order collocation methods for differential equations with random inputs. *SIAM J. Sci. Comput.*, 27(3):1118–1139 (electronic), 2005.
- [52] D. Xiu and G. E. Karniadakis. The Wiener-Askey polynomial chaos for stochastic differential equations. *SIAM J. Sci. Comput.*, 24(2):619–644 (electronic), 2002.

(A. Chertock)

DEPARTMENT OF MATHEMATICS, NORTH CAROLINA STATE UNIVERSITY

E-mail address: `chertock@math.ncsu.edu`

(A. Kurganov)

DEPARTMENT OF MATHEMATICS, SOUTHERN UNIVERSITY OF SCIENCE AND TECHNOLOGY AND MATHEMATICS DEPARTMENT, TULANE UNIVERSITY

E-mail address: `kurganov@math.tulane.edu`

(M. Lukáčová-Medvid'ová)

INSTITUTE OF MATHEMATICS, JOHANNES GUTENBERG-UNIVERSITY MAINZ

E-mail address: `lukacova@uni-mainz.de`

(P. Spichtinger)

INSTITUTE OF ATMOSPHERIC PHYSICS, JOHANNES GUTENBERG-UNIVERSITY MAINZ

E-mail address: `spichtin@uni-mainz.de`

(B. Wiebe)

INSTITUTE OF MATHEMATICS, JOHANNES GUTENBERG-UNIVERSITY MAINZ

E-mail address: `b.wiebe@uni-mainz.de`